

QATAR UNIVERSITY

COLLEGE OF ARTS AND SCIENCES

DESIGNING FLEXIBLE AND POROUS POLYSTYRENE/SILVER DOPED ZINC OXIDE

NANOCOMPOSITE FIBER SORBENTS FOR OIL/WATER SEPARATION

BY

ALI ALAA ELDEIN ALI EL-SAMAK

A Thesis Submitted to

the College of Arts and Sciences

in Partial Fulfillment of the Requirements for the Degree of

Masters of Science in Material Science and Technology

June 2020

© 2020 Ali Alaa Eldein Ali El-Samak. All Rights Reserved.

COMMITTEE PAGE

The members of the Committee approve the Thesis of
Ali Alaa Eldein Ali El-Samak defended on 05/05/2020.

Prof. Mariam Al Ali Al Maadeed
Thesis/Dissertation Supervisor

Dr. Mohammad K. Hassan
Committee Member

Dr. Samer Adham
Committee Member

Approved:

Ibrahim AlKaabi, Dean, College of Arts and Sciences

ABSTRACT

EL-SAMAK, ALI, A., Masters : June : [2020], Material Science and Technology

Title: Designing Flexible and Porous Polystyrene/Silver Doped Zinc Oxide Nanocomposite Fiber Sorbents for Oil/Water Separation.

Supervisor of Thesis: Prof. Mariam, A., Al-Maadeed.

The aim of this work is to fabricate hydrophobic porous nanocomposite with enhanced oil adsorption capacity and multifunctional features including antibacterial and photocatalytic effect. Zinc oxide (ZnO) and silver doped zinc oxide (Ag-ZnO) nanomaterials are fabricated by sol-gel method and added to polystyrene (PS) fibers which are fabricated by solvent induced phase separation process coupled with electrospinning.

The structure and morphology of the nanomaterials and polymer nanocomposites are characterized through scanning electron microscopy (SEM), tunneling electron microscopy (TEM), Fourier-transform infrared spectroscopy (FTIR), energy dispersive spectroscopy (EDS), X-ray diffraction (XRD) studies, and X-ray photoelectron spectroscopy (XPS). These techniques are capable of confirming distribution of the nanomaterials within the nanocomposite, hence highlighting the effect of the polymer/filler interfacial interactions. The significance of this work is the enhancement of the mechanical, thermal, and wettability properties of PS through the successful incorporation of the nanomaterials. These tests were carried out using universal testing machine, thermogravimetric, and optical contact angle respectively. In addition, the maximum absorption capacity of the sorbent reached 68.54 g/g, 61.23 g/g, and 58.41 g/g for mineral oil, engine oil, and olive oil respectively. In addition to displaying excellent anti-fouling resistance and photocatalytic activity, the prepared polymer

nanocomposite exhibited good mechanical strength with young's modulus amounting to 2.77 MPa, which is a sought after property in the oil/water separation related industries.

DEDICATION

This Thesis is dedicated to my family and friends for their unconditional love and support.

ACKNOWLEDGMENTS

My sincere gratitude goes first to my supervisor Professor Mariam Al-Maadeed for her expert guidance and support through my graduate education. I would also like to thank my committee members Dr. Mohammad Hassan, and Dr. Samer Adham for their advice and assistance.

To the faculty and staff at the Center for Advanced Materials, thank you, especially to Dr. Deepalekshmi for her genuine kindness, constant encouragement, and kindling my passion for research.

In addition, a thank you to the faculty members of Material Science and Technology program at Qatar University for building and expanding my knowledge in the materials field for the past 2 years.

I would like to extend my gratitude to the staff of Central Laboratory Unit, and Biomedical Research Center for their expertise and assistance in my work.

Finally, I would like to acknowledge the financial support granted by Qatar University through the Graduate Assistantship Program.

TABLE OF CONTENTS

DEDICATION.....	v
ACKNOWLEDGMENTS	vi
LIST OF TABLES.....	x
LIST OF FIGURES	xi
CHAPTER 1: INTRODUCTION.....	1
CHAPTER 2: LITERATURE REVIEW.....	5
2.1 Polymer nanocomposites.....	5
2.2 Polystyrene background.....	6
2.3 Polystyrene nanocomposites	8
2.3.1 Nanomaterials fabrication.....	8
2.3.2 Porous material fabrication.....	10
2.4 Surface wettability.....	11
2.5 Oil absorption and water treatment.....	12
CHAPTER 3: EXPERIMENTAL WORK.....	16
3.1 Materials.....	16
3.2 Sample preparation.....	16
3.2.1 Preparation of ZnO and Ag doped ZnO powders.....	16
3.2.2 Preparation of polystyrene nanocomposites.....	17

3.2.3 Electrospinning of treated polystyrene solution	18
3.3 Characterization techniques	19
3.3.1 X-ray diffraction (XRD).....	19
3.3.2 X-ray photoelectron spectroscopy (XPS).....	21
3.3.3 Fourier-transform infrared spectroscopy (FTIR).....	21
3.3.4 Scanning electron microscopy/Energy Dispersive X-ray spectroscopy SEM/EDX.....	22
3.3.5 Transmission electron microscopy (TEM).....	24
3.3.6 Mechanical properties testing.....	25
3.3.7 Thermogravimetric analysis (TGA)	26
3.3.8 Hydrophobicity test	27
3.3.9 Oil/water separation test.....	28
3.4.0 Fiber biofouling testing	29
3.4.1 Photocatalytic studies	30
CHAPTER 4: RESULTS AND DISCUSSIONS	32
4.1 Structural characterization of nanomaterials.....	32
4.1.1 X-Ray diffraction analysis.....	32
4.1.2 XPS analysis.....	33
4.1.3 FTIR analysis.....	35
4.2 Structural characterization of nanocomposites	36

4.2.1 X-Ray diffraction analysis.....	36
4.2.3 FTIR analysis.....	37
4.3 Morphological characterization of nanomaterials and polymer composites.....	38
4.3.1 SEM/TEM imaging of ZnO and Ag/ZnO nanomaterials	38
4.3.2 SEM/TEM imaging of PS and PS nanocomposites	39
4.3.3 EDX analysis	41
4.4 Mechanical stability of the polymer nanocomposite.....	43
4.5 Thermal stability of the polymer nanocomposite.....	44
4.6 Wettability of the PS and PS/Ag-ZnO nanocomposite	45
4.7 Maximum oil absorption capacity of PS and PS/Ag-ZnO nanocomposite.....	46
4.8 Recyclability of the 2 wt.% of PS/Ag-ZnO nanocomposite	47
4.9 Antifouling capability of PS and PS/Ag-ZnO nanocomposite.....	50
4.10 Photodegradation capability of PS/Ag-ZnO nanocomposite	52
CHAPTER 5: CONCLUSION	54
FUTURE WORK.....	55
References.....	56

LIST OF TABLES

Table 1. Description of PS properties.....	7
Table 2. Glass transition shift due to nanomaterials addition.....	9
Table 3. Various sorbent properties.....	14
Table 4. Electrospinning conditions for PS.....	19
Table 5. Mechanical properties of the PS and its nanocomposites containing ZnO and Ag-ZnO.....	43

LIST OF FIGURES

Figure 1. Schematic presentation of the electrospinning process	11
Figure 2. Different contact angle on a solid surface, representing the interaction between the liquid droplet and the substrate.....	12
Figure 3. The preparation of the dried xerogel before the calcination step.	17
Figure 4. The phase separation process occurring due to change in miscibility between chlorobenzene and DMSO.....	18
Figure 5. Electrospinning model TL-01.....	19
Figure 6. The geometric derivation of Bragg's law. Constructive interference occurs when the value of $a_1 + a_2$ is an integer multiplied with the wavelength.....	20
Figure 7. X-ray diffractometer model PANalytical Empyrean diffractometer.....	21
Figure 8. FTIR spectrophotometer model 760 Nicolet.....	22
Figure 9. Simplified illustration of the SEM mechanism.	23
Figure 10. Scanning electron microscope/EDX instrument, model Nova Nano SEM 4.0.	24
Figure 11. Transmission electron microscope, model TECNAI TF20.....	25
Figure 12. Universal test machines - up to 5 kN.....	26
Figure 13. Thermogravimetric analyser, Perkin Elmer model 4000.	27
Figure 14. Contact angle goniometer, OCA system model 35.	28
Figure 15. Oil/water separation set up; a) presents the set up before separation, b) presents the set up after oil capture by the test fibers.	29
Figure 16. Hemocytometer for manual cell counting	30
Figure 17. Ultraviolet/visible spectroscope, Biochrom Libra model S50.	31
Figure 18. XRD pattern of ZnO and Ag-ZnO.....	33

Figure 19. XPS spectra of ZnO and Ag-ZnO, with focus on zinc.....	34
Figure 20. XPS spectra of ZnO and Ag-ZnO, with focus on oxygen.....	34
Figure 21. XPS spectra of ZnO and Ag-ZnO, with focus on silver.....	35
Figure 22. FT-IR curves of nano Ag-ZnO.....	36
Figure 23. XRD pattern of pure PS and Ps/ZnO-Ag nanocomposite.	37
Figure 24. FT-IR curves of PS and PS/Ag-ZnO nanocomposites.	38
Figure 25. SEM images of a) ZnO and b) Ag-ZnO; TEM images of c) ZnO and d) Ag-ZnO.....	39
Figure 26. SEM images for the a) PS and PS nanocomposites b) with 2 wt.% ZnO, c) with 1 wt.% Ag-ZnO d) with 2 wt.% Ag-ZnO and e) 3 wt.% Ag-ZnO	41
Figure 27. Energy dispersive spectra and EDX images for 2wt.% PS/ZnO and 2wt.% PS/ZnO-Ag nanocomposites.....	42
Figure 28. TGA curves for the PS and its nanocomposites; inset shows the onset of degradation and the derivative thermograms.....	44
Figure 29. Water contact angle values for the PS and PS nanocomposites.....	46
Figure 30. Oil absorption values for the PS and PS nanocomposites.....	47
Figure 31. Repeatability of oil separation performance by 2 wt.% of Ag-ZnO for 5 consecutive cycles.....	49
Figure 32. SEM images of a) PS and b) 2 wt.% of Ag-ZnO wetted in oil; c) PS and d) 2 wt.% of Ag-ZnO washed with NaOH.....	49
Figure 33. a) control, b) 2 wt.% of Ag-ZnO after bacterial growth. Inset shows the bacteria grown samples.....	50
Figure 34. a) bacterial cells grown on control filter and PS/Ag-ZnO, b) example of stained bacteria under 60x magnification.....	51

Figure 35. a) The concentration changes of rosindulin at 528 nm in presence of 2 wt.%
Ag-ZnO b) The change in concentration of rosindulin solution in the presence of 2 wt.%
Ag-ZnO.....53

CHAPTER 1: INTRODUCTION

Polymer based materials are widely utilized due to their distinctive properties, such as lightweight, ductility, and ease of production. Since polymers lack strength and high modulus in comparison to metals and ceramics, micro/nano materials are often added to them to enhance their properties. The inclusion of materials into a polymeric host to enhance their properties and provide new modified ones has extensive research interest. Therefore, a new class of materials has emerged, known as Polymer Nanocomposites (PNC). Typically, the nanomaterials, which are introduced to polymers have dimensions in the range of 1-100 nm. Nanoscale reinforcements provide elevated properties through the increase of mechanical strength, chemical durability, thermal stability, and novel behavior such as anti-bacterial effect, electric conductivity and photocatalytic activity [1, 2].

Polystyrene (PS) is a class of amorphous thermoplastic polymers which is easily fabricated with molecular weight (M_w) ranging between 100,000-400,000 g/mol [3]. The increase in M_w reinforces the tensile strength and elongation at break [3], these properties coupled with the malleability, chemical stability, and wettability is what allows PS to stand as one of the best polymers for oil/water separation. Furthermore, PS mimics the lotus leaf *Nelumbo nucifera* [4], which is a natural material that exhibits super hydrophobic capabilities, with water contact angle greater than 150° , while its oleophilic property is shown through its interaction with organic solvents, such as hexane with contact angle of $\sim 0^\circ$ [5]. The high hydrophobicity will allow PS to interact with oil and water differently through retaining oil, and allowing water to move freely through the polymer matrix. Additionally, wettability of the material is highly dependent on two main features, 1) the surface tension of the liquid, and 2) the geometry and surface chemistry of the material [6, 7]. The latter property can be effortlessly

manipulated in the case of PS, depending on the technique used to fabricate the polymer. Current research established the usage of PS as a successful oil sorbent. However, for PS to be considered as a potential oil-water separator, it must also have high uptake capacity, durability in aqueous media, reusability, and recoverability of absorbed oil.

In this thesis, we report the importance of nanomaterials addition to fabricate PS nanocomposite fibers. The metal oxide nanoparticles include zinc oxide (ZnO with ~ 50 nm average size) and silver-doped zinc oxide (Ag-ZnO with ~ 50 nm average size). The nanocomposites were fabricated using straightforward nonaqueous sol-gel route and the electrospinning technique. The reason behind utilizing the aforementioned materials in this project is due to the reported fiber formation and high oil absorption properties of PS. In order to improve the oil/water separation efficiency and oil absorption capacity, we opted to utilize ZnO and Ag due to their non-toxic, low cost, anti-bacterial and photocatalytic properties. Additionally, electrospinning was utilized due to its importance in fabricating highly porous fibers through the mixed solvent method, which dissolves PS in chlorobenzene and dimethyl sulfoxide solvents to form a rather uniform and highly porous structure. The porous structure imparts the high hydrophobic surface of the fibrous mats, thus increasing the oil selectivity of the fibers while repelling water.

In fact, the synthesis of non-agglomerated ZnO within the polymer matrix was only possible due to the sol-gel method. ZnO is known for its application in photocatalysis due to its physical and chemical stability, low toxicity and production cost, and high oxidative capacity [8-10]. To the best of our knowledge, this is the first time silver doped ZnO is added to PS matrix as a filler to provide mechanical, thermal, and chemical stability, in combination with anti-bacterial and photocatalytic activity.

The addition of Ag is known to enhance the photocatalytic activity of nanocrystalline photocatalysts due to its electronic and optical properties [11, 12]. Furthermore, Ag is also known for its anti-bacterial activity through its strong inhibitory and bactericidal effect, leading to a decrease in biofouling rates faced by common oil/water separators [13].

Generally, the fabrication of efficient polymer nanocomposites (PNC) is challenging, especially in retaining the beneficial polymer properties and optimizing the addition of nanomaterials to enhance current properties and provide novel ones. To produce a highly sorbent polymer matrix, it must consist of a uniform and macro/nanoporous structure, which in turn increases roughness, leading to a superhydrophobic surface [14]. In the case of strong, stable, and efficient PNC, the nanomaterials must be well dispersed within the matrix [15]. The dispersion level relies heavily on the agglomeration factor of the fabricated nanoparticles [16]. Therefore, a concentration ranging from 1-3 wt.% of ZnO/Ag hybrid nanomaterial was selected [17]. It is expected that this range of nanomaterials is optimal for the increase in mechanical and thermal stability, while also providing new anti-bacterial and photocatalytic properties. As shown by Georgekuttyl et al. [17] the fabrication of ZnO doped with a Ag percentage higher than 3 wt.% will cause an increase in the crystallite size of the Ag particle in comparison to the ZnO. This leads to poor integration and agglomeration of the nanomaterials. The advantages behind filler modifications such as doping consists of strong effect on structural integrity, and increase in morphological properties, yet the addition of the fillers must be optimized to ensure maximum benefit without hindering the polymer matrix [18].

We have successfully fabricated doped PS polymer nanocomposite through a two-stage fabrication process. The first stage consisted of synthesizing the

nanomaterials using simple sol-gel method; the second stage consisted of utilizing the electrospinning technique to produce uniformly dispersed PNC, the combination of both methods highlights the efficiency to generate less aggregated nanoparticles and porous fibrous composite. The produced material possessed higher thermal stability, uniform morphology, mechanical strength, higher hydrophobicity, and an increase in sorption capacity in comparison to plain PS. The composites also showed strong photocatalytic and anti-bacterial functions. Moreover, nanomaterials also increased the Young's Modulus and elongation at break of the PS polymer matrix. The improved hydrophobicity, mechanical strength and anti-bacterial activity of the fabricated PNCs could permit their utilization as sorbents or membranes in wastewater treatment application with great potential.

CHAPTER 2: LITERATURE REVIEW

2.1 Polymer nanocomposites

The last decade witnessed an increase in number of nanomaterials reported in the scientific literature. Their presence within a polymer, even with very low quantity, can lead to substantial property enhancement, and possible development of new properties. Nanomaterials are defined as materials with at least one of their dimensions in the nanoscale (1 nm to 100 nm). They are generally divided into layers (1 dimensional), tubes (2 dimensional), and particles (3 dimensional), depending on the number of dimensions they possess at the nanoscale [19]. PNCs are a class of materials comprising of a mixture of two or more materials (one is in nano dimension) with separated crystal phase. PNCs can be applied also as a coating layer through its deposition on selected substrates to behave as a supportive entity [20, 21]. PNCs are used commercially due to their enhanced properties, with their most common form being nanoclays, which was firstly used by Toyota as nylon 6-clay in their hybrid car systems [22]. Nano-oxides represent another viable class of nanomaterials that was studied extensively in literature, including ZnO, TiO₂, and SiO₂ and are commonly used to provide UV protection, self-cleaning, and tailored geometrical structures [23]. The performance of nanomaterials largely depends on the multiple nanoparticles' features, including size, aspect ratio, surface area, compatibility and dispersion within the used matrix; however, lower filler loading of nanoparticles is always preferred [24]. Although, all aforementioned parameters are important, the extremely high surface area is the leading factor in changing the composition gradient, crystallinity, and mobility charge of the PNCs, leading to an enhanced overall performance of the designed material [25]. Polymers also adhere to a set of requirements to produce a successful PNC. The two main requirements are a) good compatibility between the polymer and the nanoparticle surface (optimum surface tension), and b) maximum dispersion of

nanoparticles within the polymeric surface. These requirements can be achieved through low agglomeration, similar surface energy of the polymer matrix and the nanoparticles, low polymer viscosity, and high mixing efficiency [24].

2.2 Polystyrene background

PS was the first fabricated synthetic polymer, and one of the most in demand thermoplastics globally [26]. It is an aromatic hydrocarbon polymer, with a monomeric base of styrene (vinyl benzene). The physical characteristic of PS includes brittleness and hardness and it is fabricated as either solid or foam. The combination of low price per unit weight, and the ability to polymerize styrene through all known mechanisms (radically, anionically, and cationically) is what makes PS a lucrative thermoplastic in the global market [27]. General property description of PS is shown in table 1 [27].

The discovery of PS took place in 1839, by German scientist Eduard Simon, through the extraction of resin from *Liquidambar styracifua*, an American sweetgum tree. The 1940's witnessed the first commercial use of PS through the production of Styrofoam as it is stable, lightweight, and an insulator [28]. To overcome the initial brittleness of PS, Ostromislensky and Coworkers decided to incorporate polybutadiene within its structure in the 1950's to produce what is known as impact modified polystyrene (IPS). This commercialized a tougher PS, with multiple small cracks within its structure to absorb high energy forces [29, 30].

Table 1. Description of PS properties.

Property	Unit	Value
Density	g cm ⁻³	1.05
Glass transition temperature	°C	100
Tensile strength	kPa	230-330
Elongation at yield	%	1.5-3.0 %
Water absorption when immersed in water after 7 days, after 28 days	vol. %	0.5-1.5, 1.0-3.0

The first usage of PS resins as a sorbent was reported in 1963, where Ayerts et al. patented sulfonated PS resins that allow the removal of metal contaminants from petroleum oil. These metal contaminants in crude oil presents an undesirable feature. Therefore, the usage of PS as a granular resin allowed the removal of metal complexes including nickel and vanadium through salt formation on the surface of the PS sorbent [31].

Kondoh et al. [32] fabricated synthetic polymer suitable for waste water treatment, by removing oils floating on the water surface. The research was based on the difference in contact angle between the polymer and oil/water. The wider contact angle between the water and polymer does not allow water sorption, while the narrower contact angle between oil and polymer allowed oil adhesion on the polymer surface. PS was one of the main polymers Kondoh's research group suggested for oil removal as preliminary records proved total oil removal from the surface of the water.

Zhu et al. [33] reported the fabrication and design of polyvinylchloride (PVC)/PS oil sorbent by the electrospinning method. The fabricated sorbent achieved a sorption capacity 9 times higher than that of commercially used polypropylene sorbent. The sorption mechanism can be attributed to adsorption and absorption mechanisms, as the adhesion of the oil particles can be found within the voids and on

the surface of the sorbent. Lin et al. [34] also developed PS fibers for oil spill clean-up and sea water treatment through electrospinning process and the fibers separated sea water from motor oil at a capacity of 113.87 g/g. This was slightly lower than the achievements from Zhu's group, who recorded a motor oil sorption of 146 g /g. Lin, proved that it is possible to use PS alone as a sorbent for oil removal while still achieving high sorption values. His work showed that PS fibers with a smaller fiber diameter and smoother surface have higher sorption capacity, in comparison to PS fibers with a larger fiber diameter and rough surface. However, both groups neglected the need of mechanical robustness and reusability, which is a crucial aspect to oil/water separating devices in the industry.

Wu et al. [35] presented the first doped PS fiber for oil removal application, demonstrating superhydrophobic and oleophilic properties. The carbon nanotubes doping exhibited an increase in sorption capacity and reusability for the fibers which is attributed to the enhanced fiber characteristics provided by introducing CNTs to the matrix. These properties included increase in porosity, surface area, water contact angle, reusability and oleophilic nature of the PS fiber with maximum sorption capacity of water oil at 112 g/g. Yet, the need of an anti-bacterial oil/water separator remains unanswered, hence bacteria found in oil/water emulsion lead to quick membrane deterioration.

2.3 Polystyrene nanocomposites

2.3.1 Nanomaterials fabrication

Nanomaterials can be used to modify the polymer's properties. Nanomaterials must have at least one of its dimensions in the nanoscale, while its morphology vary from tubular, spherical, to flower-like shapes [36]. For instance, the addition of trace amounts of iron oxide nanoparticles increases the oil absorption capabilities of a polymer through the reduction of surface repulsive forces [37].

Other forms of nanoreinforcements have been explored in literature, providing mechanical, thermal and chemical stability. One of the highly used nanomaterial is carbon nanotubes (CNT) as its crystallographic structure allows it to act as a filtrate for a wide range of water pollutants, including toxic metal traces and oils [38]. The increase in stability of polymeric matrix reflects in the increase in glass transition temperature. This indicates an increase in crystallinity of the polymer. Table 2 shows the different nanocomposites and their effect on the crystallinity of its polymeric host.

Table 2. Glass transition shift due to nanomaterials addition

Polymer	Nanofiller	T _g change	Reference
Polystyrene	single walled CNT	3	[39]
Polydimethyl siloxane	Silica (2.5 nm)	10	[40]
Polypropylene carbonate	Nanoclay (4 wt%)	13	[41]
Polyimide	Multi walled CNT (1-6 wt%)	4 to 8	[42]

In general, metal oxide nanomaterials are well established in the field of research due to their surface modification capabilities, mechanical properties, and high surface area. ZnO is a primary example of functional nanomaterial that has been incorporated successfully into polymeric matrices. Additionally, ZnO is relatively cheap with very low toxicity values [43]. Different fabrication methods for ZnO include coprecipitation [44], chemical vapor deposition (CVD) [45], and sol-gel methods [46]. Although, the coprecipitation method allows uniform particles distribution, it also increases the impurities induced by the different melting points of the starting materials [44]. CVD is also an advanced method that allows for the design of unique ZnO nanoparticles. However, it is a fabrication technique that requires multiple complex steps, sophisticated equipment, and rigorous experimental set up [47].

By using the sol-gel method, the fabrication of ZnO nanoparticles is considered low-cost, reliable, repeatable and simple [48]. In comparison to the aforementioned techniques, sol-gel method is straightforward and it allows improved control of the particle morphology through hydrolysis and condensation reactions [49]. The sol-gel method starts with the hydrolyzation of metal organic reactants in an organic solvent, followed by the condensation of the hydrolyzed species with either water or alcohol. The drying of the reactants at ambient conditions produce xerogel, which is calcined at optimal temperature to decompose to nano particles.

2.3.2 Porous material fabrication

PS is a polymer with multiple synthetic routes, depending on the property, morphology, and application needed. It can be polymerized through anionic, cationic, and radical polymerization. Its preparation as an effective sorbent for water treatment can be initiated through extrusion, melt-spinning, wet-spinning, and electrospinning [50-52]. While both melt and wet-spinning are capable of preparing PS fibers with interesting structure feature, they still require multiple stages for the PS sorbent to achieve the application stage. Secondary and usually tertiary treatment are needed to obtain the required structure, such as coagulation, stretching, washing, casting, and drying [53]. On the other hand, electrospinning requires no further preparation steps, as it is a simple and direct technique used to produce fiber mats to utilize within oil/water treatment applications.

Electrospinning is a versatile technique to fabricate continuous fibers ranging from nanometers to micrometers in diameter [54, 55]. Additionally, the simplicity of the electrospinning process and controllable feature of the fabricated fiber highlights the appeal of it as a technique for oil sorbent fabrication [56].

The electrospinning process begins with applying high voltage to polymer

solution in order to manipulate its surface tension. After reaching a certain voltage threshold, the polymer solution morphs into a semicircular surface known as the Taylor Cone [57-59]. The ejected solution consequently forms a direct path, which is further stretched due to the instability caused by the presence of the collector leading to the dissolution of the liquid into fiber. Applied voltage, flow rate, polymer viscosity and the distance between the needle and the collector are all factors that affect the size and morphology of the fabricated fiber [60]. This process is clearly demonstrated in Figure 1 [61-67].

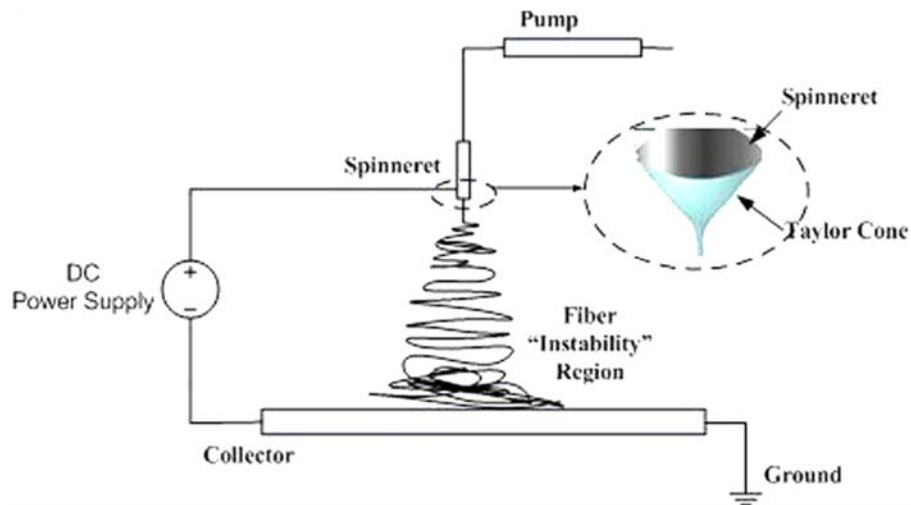


Figure 1. Schematic presentation of the electrospinning process

2.4 Surface wettability

Fabricating materials with an optimized high wettability characteristic has great significance in the separation of oil and water [68]. The wettability of a solid surface represents a macroscopic interaction between the liquid and the substrate material. Wettability is measured by quantifying the contact angle (CA), of a liquid drop on a solid surface and air medium as seen in Figure 2.

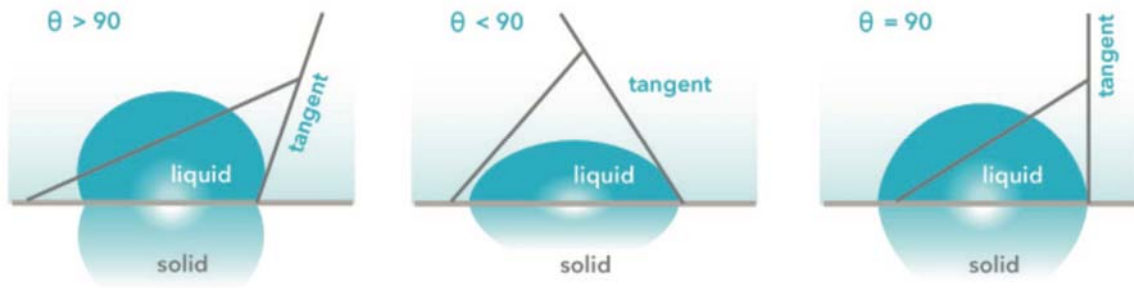


Figure 2. Different contact angle on a solid surface, representing the interaction between the liquid droplet and the substrate.

A substrate is considered hydrophobic if the water contact angle is above 90°, and hydrophilic if the water contact angle is below 90°. In the case of certain substrates such as sorbents and membranes, special wettability is used to describe the solid/liquid interaction.

For example, the material is super hydrophobic when it is extremely repellent to water [69], and superoleophilic when the material is highly adhesive to oil [70].

The most common technique for studying the mechanism behind wettability is the usage of Young's equation:

$$\gamma_{SG} - \gamma_{SL} - \gamma_{LG} \cos\theta = 0 \quad (1)$$

The equation is used when the substrate is homogeneous with a smooth surface, it calculates the contact angle based on the surface tension between solid and liquid γ_{SL} , between solid and gas γ_{SG} , and between liquid and gas γ_{LG} [71]. The aforementioned equation can be derived through minimizing the interfacial Gibbs free energy, or through balancing the air/liquid/solid triple phase boundary line.

2.5 Oil absorption and water treatment

Wide range of materials can be employed as oil spill reducers, including adsorbents, solidifiers and boomers [72]. Whereas flotation, centrifugation, membrane

separation and absorption are applied in wastewater treatment [73]. Absorption is a flexible technique that is applied to a variety of water treatment applications. For example, Sokker et al. [74] concluded that chitosan based polyacrylamide hydrogel was successful at removing oil from aqueous solution at pH ~ 3 with absorption capacity of 2.3 g/g, , albeit less absorption (1.8 g/g) capacity of crude oil within seawater. The decrease in the latter case is attributed to the effect of various cations present in seawater, leading to difference in osmotic pressure and absorption tendency. Table 3 summarizes different studies on sorbent materials.

Table 3. Various sorbent properties.

Type of sorbent	Structure	Type of oil	Sorption capacity g/g	Reusability	References
Clay	Granular	Diesel, and hydraulic oil, Engine oil	5.2-7.2, 2.2-3.6, 2.1-3.6	no	[75]
Polypropylene	Porous discs	Crude oil, and petroleum products	10.1-16	30 cycles	[76]
Butylrubber	Macroporous gel	Crude oil, and olive oil	33-38, 24-27	20 cycles	[77]
Walnut shell media	Granular	mieral oil, vegetable oil, bright-edge oil	0.56, 0.58, 0.74	yes	[78]
Cotton fibre	Fibre	Crude oil, and tested on water surface and separately in oil bath.	30-40	3 cycles	[79]

Li et al. [80] fabricated superhydrophobic microporous polymers with high selectivity. The open pore structure and high surface hydrophobicity of the polymer allowed the removal of oil and non-polar solvents, with no water absorption. Oil absorption can be calculated using the following equation (2).

$$Q = \frac{m - m_o}{m_o} \quad (2)$$

The oil absorption capacity is presented as Q , m represents the weight after

absorption, m_o represents the original sorbent weight. The mechanism behind oil/sorbent interaction can be classified into two; absorption and adsorption. While the latter refers to surface interaction, which is attributed to the accumulation of oil on the liquid/solid surface, the former mechanism involves the penetration into the sorbent material, especially for porous or hollow structure [81]. It is believed that both scenarios can occur simultaneously. Wahi et al. [82] suggest that the main absorption mechanisms occurring within porous structures are diffusion, agglomeration, and capillary action. Capillary action is mainly found in sorbents with hair like features, as the sorbate uses intermolecular forces to travel because of capillary pressure and surface tension [83]. The nanocomposites proposed in this work mainly follow both of these mechanisms and act as better oil absorbers, thus efficiently separating oil from contaminated water samples. Additionally, this work focuses on overcoming the limitation of previously reported work, hence it is clear from table 3 that most oil sorbents currently utilized either have a low sorption capacity or a low reusability, therefore the aim of this work is to overcome that gap through producing a reusable fiber nanocomposite with a high oil absorption capacity.

CHAPTER 3: EXPERIMENTAL WORK

This chapter introduces the materials used in the preparation of the nanoparticles and the nanocomposite porous fibers. The first section of this chapter outlines the procedures and methods used to produce the samples, including nonaqueous sol-gel method to prepare nanomaterials and electrospinning to prepare the final PNC fibers. The second section will discuss the characterization techniques used to evaluate the structural, morphological, mechanical, thermal, photocatalytic, antibacterial and oil sorption capabilities.

3.1 Materials

Zinc acetate dihydrate, silver nitrate, oxalic acid, ethanol, chlorobenzene and dimethyl sulfoxide (DMSO) were purchased from Sigma Aldrich. Polystyrene (PS, Mw ~350000 g/mol) pellets were also commercially obtained from Sigma Aldrich. All the reagents and chemicals were used as such without any additional chemical treatments.

3.2 Sample preparation

3.2.1 Preparation of ZnO and Ag doped ZnO powders

Sol-gel is a nonaqueous process which promotes the production of controlled and uniform metal oxide nanoparticles in organic solvents [84]. Firstly, 2.75 g of zinc acetate was dissolved in ethanol (125 mL) at 60 °C for 30 minutes. A second solution consisting of 3.14 g of oxalic acid was dissolved in ethanol (50 mL) and was slowly added to the zinc acetate solution. The mixture was stirred for 2 h, forming a thick white colloidal semi-gel, which was left to dry overnight at 80 °C. The dried residue was further calcined at 400 °C for 2 hours at a 5 °C per minute increment using a box furnace to produce the ZnO powder, as seen in Figure 3 [17]. The same procedure was followed with the addition of 2 wt. % of silver nitrate to the second solution to prepare Ag doped ZnO powder.

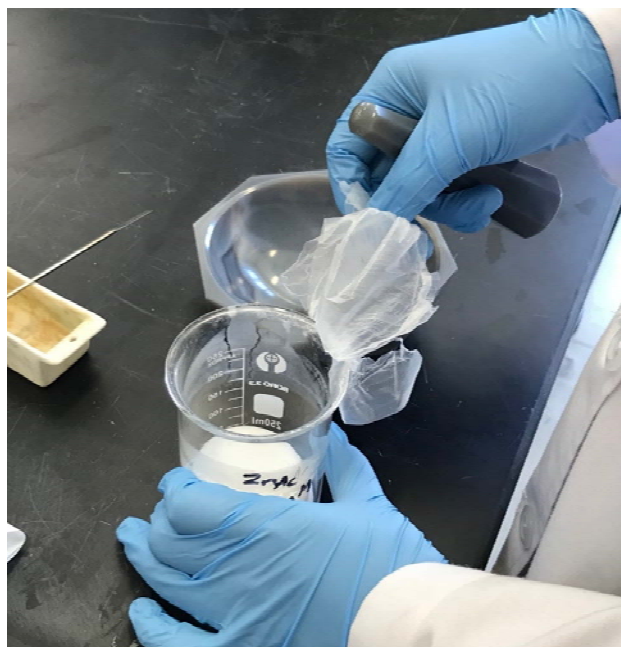


Figure 3. The preparation of the dried xerogel before the calcination step.

3.2.2 Preparation of polystyrene nanocomposites

A series of PS solutions comprising of different concentrations of nanocomposites (1 wt.%, 2 wt.%, and 3 wt.% weight per volume) were prepared following the work of Chen et al. using nonsolvent-induced phase separation (NIPS) [14]. The specific concentrations are adopted by considering the reported percolation threshold values as beyond 3 wt.% the nanomaterials tend to agglomerate within the polymer which limits their enhancing effects. This method involves premixing nonsolvent polymer solutions at a specific concentration that does not cause phase separation until the electrospinning stage. Once the electrospinning begins, the phases separate due to change in volatility between solvent and non-solvent, forming a porous structure as seen in Figure 4 [85, 86]. The solutions consisted of 300 mg/ml of PS that dissolved in a chlorobenzene and dimethyl sulfoxide cosolvent, at a 7 mL to 3 mL ratio. The final solution was magnetically stirred for 12 h at 60 °C. Once the solution was homogenized, the nanoparticles at specific concentration predispersed in the same solvent by bath sonication (60 min) were added and magnetically stirred at 350 rpm

overnight.

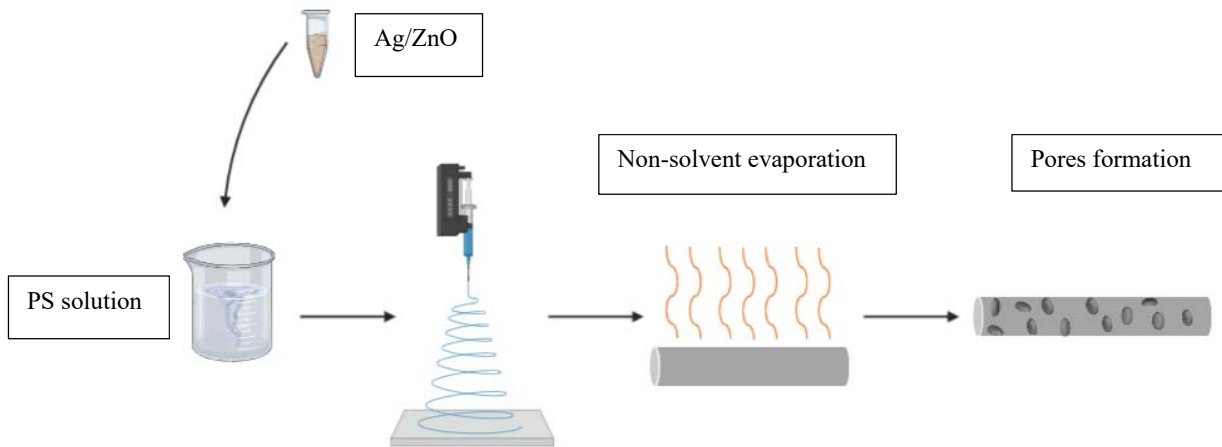


Figure 4. The phase separation process occurring due to change in miscibility between chlorobenzene and DMSO.

3.2.3 Electrospinning of treated polystyrene solution

The electrospinning operation was carried out by TL-01 model which is shown in Figure 5, purchased along with its accessories from Tong Li Tech, China. The electrospinning process involves utilizing repelling electrostatic forces to overcome the surface tension force of the



Figure 5. Electrospinning model TL-01.

polymeric solution, causing the liquid ejected from the spinneret to form a continuous fine thread [87]. The polymeric fiber fabrication was done at atmospheric pressure and at room temperature. The solution was ejected at a controlled feed rate using syringe pump with a needle size of G23 as a spinneret. The fibrous mat was collected on an aluminum foil attached to a flat metal collector. The process was concluded, once 5 mL of the electrospun solution was converted to fiber. Table 4 presents all the common variables. These parameters were used due to their success in previous works to form the highest distribution of pores within PS fibers.

Table 4. Electrospinning conditions for PS

Parameter	Value
Concentration	30% w/w
Flow rate	0.7-1.0 mL/h
Voltage	10.0-12.0 KV
Temperature/pressure	ambient
Distance	15 cm

3.3 Characterization techniques

3.3.1 X-ray diffraction (XRD)

X-ray diffraction is a high-resolution, non-destructive, analytical technique that is limited to an absorption depth of 10 μm . It determines the phase identification of crystalline material and studies the influence of different preparation methods on the lattice constant [88]. The strongest form of constructive diffraction interference occurs when the incident electromagnetic radiation is in the same phase as the interatomic distance (d) in the lattice structure; which is known as Bragg's law as seen in Figure 6.

$$n\lambda = 2d_{hkl} \sin\theta \quad (3)$$

Equation 3 represents the Bragg equation, where λ is the wavelength of the radiation, θ is the angle between the lattice and incident beam, while n is an integer number [89].

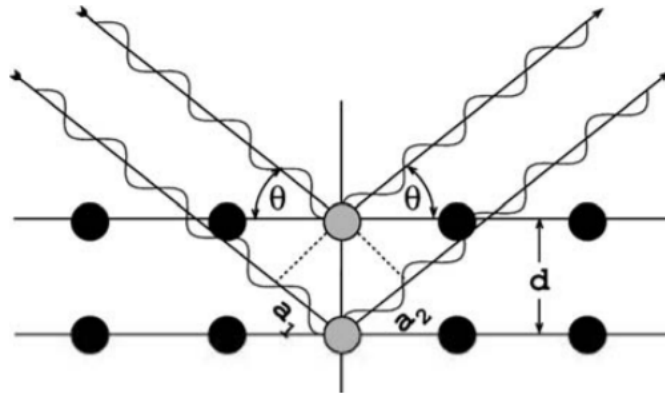


Figure 6. The geometric derivation of Bragg's law. Constructive interference occurs when the value of $a_1 + a_2$ is an integer multiplied with the wavelength.

The XRD technique was used to analyze both nanomaterials and nanocomposites. In this work used PANalytical Empyrean diffractometer was used as seen in Figure 7, generating X-ray through a copper anode with $K\alpha$ of 1.54 nm wavelength. The scattering angle was measured from 10° to 90° at a scan step size of 0.013° per minute. The applied voltage was 45 V and the tube current was 40 mA.



Figure 7. X-ray diffractometer model PANalytical Empyrean diffractometer.

3.3.2 X-ray photoelectron spectroscopy (XPS)

X-ray photoelectron spectroscopy is a sensitive quantitative technique used to determine the elemental composition, empirical formula and electronic state of the samples. The detection depth of this technique is between 1-10 nm, and it is initiated through the irradiation of X-rays in ultrahigh vacuum conditions. Followed by using a spectrometer as a detector to determine the kinetic energy and number of excited electrons, plots are made from intensity signal as a function of the samples' binding energy [90]. Around 5-10 mg of the prepared nanomaterials samples were placed within the instrument, which were then tested at ultra-high vacuum under 10^{-8} torr), leading to the generation of high resolution spectrum of intensity varying with binding energy (eV), hence the binding energy is considered a finger print like property which is unique to each element.

3.3.3 Fourier-transform infrared spectroscopy (FTIR)

FTIR is an analysis techniques which determines the compounds present within

the sample based on an IR absorbance range from (4000 – 400 cm^{-1}). The instrument used in this work is the 760 Nicolet FTIR model as seen in Figure 8, which enabled the determination of organic and inorganic function groups based on their unique IR frequency.



Figure 8. FTIR spectrophotometer model 760 Nicolet.

3.3.4 Scanning electron microscopy/Energy Dispersive X-ray spectroscopy SEM/EDX

Scanning electron microscope is a microscope that uses focused electron beams instead of light, to scan the surface of the sample, and produces an image with an extremely high resolution. Electron/sample interaction produces different forms of signals with the most important signal produced from the backscattered secondary electrons (SE). SE reveals multiple characteristics, including surface topography, chemical composition and morphology [91].

Energy Dispersive X-ray spectroscopy EDX is an accessory included in most modern SEMs. Its objective entails exciting an inner shell electron from the sample by

bombarding it with an electron beam which is demonstrated in Figure 9. Subsequently, causing an electron from a higher energy shell to substitute the previously excited electron. Leading to a fingerprint signal formed by the electron traveling between shells, EDX is capable of depicting the results in both spectrum and map form [92].

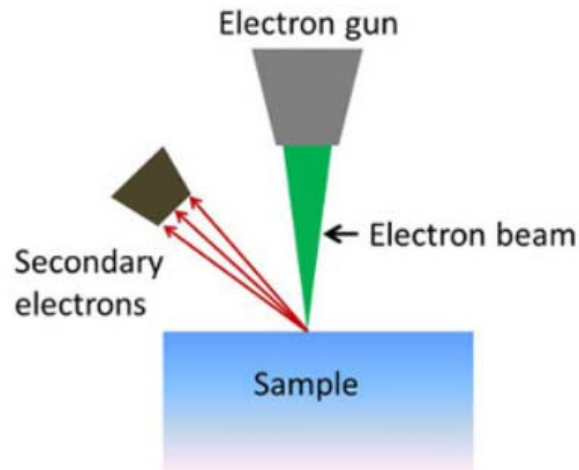


Figure 9. Simplified illustration of the SEM mechanism.

The SEM instrument used in this work was Nova Nano SEM 450 as seen in Figure 10 with a voltage capability ranging from 200 V to 30 kV. The fiber samples required pre-treatment which included sputtering a thin layer of gold particles on the surface to increase the interaction between the beam and the sample.



Figure 10. Scanning electron microscope/EDX instrument, model Nova Nano SEM

4.0.

3.3.5 Transmission electron microscopy (TEM)

Transmission electron microscopy is another form of microscopy technique. The sample should be with a thickness less than 100 nm. The morphology of the sample is observed with TEM by the transmittance of the electron through the sample. The resolution of this technique is up to 0.1 nm, which enables the investigation of the lattice crystal at the atomic scale. Bright field is the common imaging mode used to determine defective and structural changes at the atomic scale. However, the dark field can also be used and both imaging modes determine amplitude and diffraction, contrasting within the sample [93].

TECNAI G2 TEM, TF20 model was used in this work as seen in Figure 11, to confirm the morphology, structure, and to determine the change in lattice parameters when different nanocomposites were prepared. The samples were placed on a 3 mm copper grid, followed by the bombardment of electrons by Argon ions accelerated at 200 kV.



Figure 11. Transmission electron microscope, model TECNAI TF20.

3.3.6 Mechanical properties testing

The mechanical properties of the fibers were tested using Lloyd materials testing instrument by AMETEK as seen in Figure 12. The elongation, tensile strength, and Young's modulus were automatically calculated through the universal test machines. The fiber was cut into a rectangular 2 cm x 5 cm dimensions, 0.7 mm average thickness and placed between both holders. The sample was pulled at a constant rate of 2 mm/min, thus generating a strain Vs. stress graph that enables the derivation of the aforementioned mechanical properties [94].



Figure 12. Universal test machines - up to 5 kN.

3.3.7 Thermogravimetric analysis (TGA)

Thermogravimetric analysis is a form of thermal analysis that measures the change in mass over time as a function of temperature increase. This technique can be used to assess multiple characteristics, including phase transition, thermal decomposition and solid/gas reactions [95].

Perkin Elmer TGA4000 thermogravimetric analyzer was used as seen in Figure 13 at a temperature ranging from 30 °C to 800 °C, with a constant temperature increase at a rate of 10 °C per minute. The aim is to record the maximum temperature at which

the fiber samples can withhold their chemical composition before degrading.



Figure 13. Thermogravimetric analyser, Perkin Elmer model 4000.

3.3.8 Hydrophobicity test

The degree of hydrophobicity was evaluated through determining the contact angle measurements according to the sessile drop method. The Young-Laplace model was used to determine the contact angle, which is directly correlated to the surface roughness of the prepared samples [96], using the OCA35 system as seen in Figure 14, in addition to CCD camera, which were required to capture the droplet accumulation on the samples surface. Up to 3 μL of water was placed above the sorbent sample, followed by a 3-second grace period before the contact angle was calculated, to allow for the thermodynamic equilibrium between the sample and the droplet to be achieved. The tests were repeated at least 3 times at different locations on the substrate to determine the mean value for the contact angle of the substrates, this test was conducted to determine the change in hydrophobicity which directly correlates to the change in surface roughness of the test samples [14, 97].

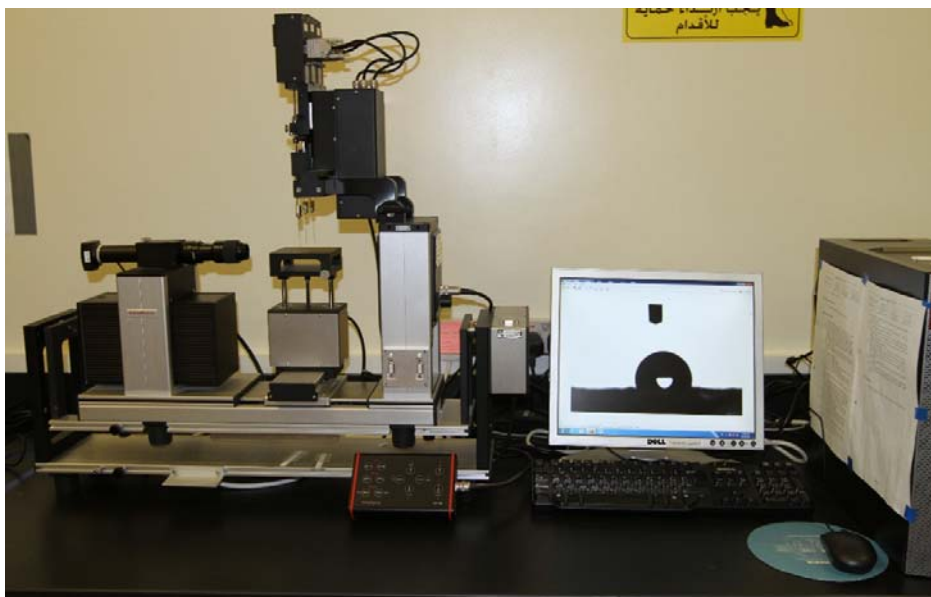


Figure 14. Contact angle goniometer, OCA system model 35.

3.3.9 Oil/water separation test

The oil/water separation test consisted of preparing engine oil with a concentration of 50 ppm to replicate oily conditions of industrial wastewater. The solution was sonicated and heated to allow for homogeneity of oil in water. The separation was carried out as seen in the set up in Figure 15, the fiber used had a thickness of 15 mm, with an external pump allowing 5 ml/s flow rate of the solution. Sorbent recyclability was also tested with multiple separation sessions on the same fibrous PS nanocomposite. The organic content of the solution was analysed using the total organic carbon (TOC) instrument, model TOC-L, from Shimazu, China.

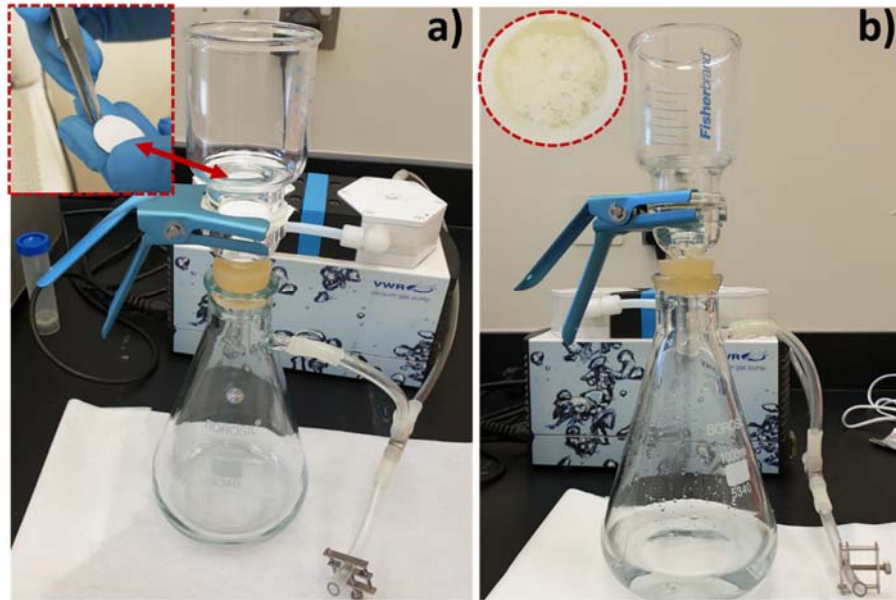


Figure 15. Oil/water separation set up; a) presents the set up before separation, b) presents the set up after oil capture by the test fibers.

3.4.0 Fiber biofouling testing

The antibacterial properties of the fibers were tested using common bacteria, *Staphylococcus aureus*. The bacteria was lab grown according to the research of Sabri et al. [98] followed by the incubation of the membrane samples within the bacterial solution for 24 h at 37 °C. Further preparation steps were done through membrane analysis using SEM characterization, such as paraformaldehyde cross-fixing, to ensure the preservation of the cells morphology. The bacteria was diluted 5 times, suspended and stained with 4 µg/ml 4,6-Diamidino-2-Phenylindole (DAPI). DAPI is a specific stain for DNA in cells, which offers better detection and certainty. Therefore, the stained bacterial suspension was counted using a hemocytometer as seen in Figure 16, by injecting 10 µl of the sample inside the hemocytometer groove. Cells in the middle hemocytometer squares were manually counted at 60X magnification using Olympus fluorescent microscope, and the average number of cells was obtained through equation 4:

$$\text{Total cell count } \left(\frac{\text{cells}}{\text{ml}}\right) = \quad (4)$$

*average number of cells * dilution factor * hemocytometer constant*

The total cell count represents an estimation of the amount of cells grown on the polymer nanocomposite material, the average number of cells represents the cells counted using the microscope, the dilution factor used in this experiment was a factor of 5, and the hemocytometer constant is 10^4 .

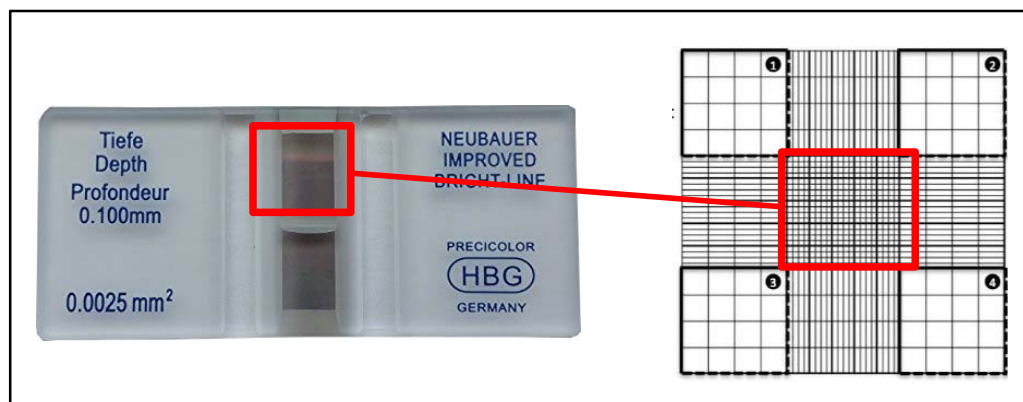


Figure 16. Hemocytometer for manual cell counting

3.4.1 Photocatalytic studies

The UV-Visible spectroscopy is an analytical technique used for quantitative measurement of wide range of chemicals, including transitional metals and conjugated organic compounds. This instrument is capable of detecting chemicals found in the electromagnetic spectrum, from a range of 200-400 nm (ultraviolet range) and 400-800 nm (visible range) [99]. The purpose of this instrument is to determine the effectiveness of the prepared samples in degrading common toxic organic compounds, through monitoring the reduction in concentration of the organics with respect to their exposure time to the prepared samples through equation 5:

$$A = \epsilon cl \quad (5)$$

Where A represents the absorbance transmitted by the sample, ϵ is the molar absorption coefficient, c is the molar concentration and l is the optical path length. Both

c and l are constants, therefore the change in absorbance will have direct correlation to the change in concentration of the test subject.

The photocatalytic efficiency of the polymer nanocomposite was evaluated through the degradation of rosindulin dye. The experimental details were as follows: 10 mg of fibrous material was placed in a 50 mL beaker of 10 mg/L rosindulin aqueous solution. Followed by reaching adsorption equilibrium through placing the mixture in the dark for 1 hour. Subsequently, the solution was irradiated under direct sunlight for a period of 6 hours, while 4 ml was withdrawn from the solution after each hour. The UV/Visible spectroscopy was carried out via (Biochrom libra model S50) seen in Figure 17, at the range of 300-600 nm. With an average sunlight intensity of 70,000 – 90,000 lux striking the solution.

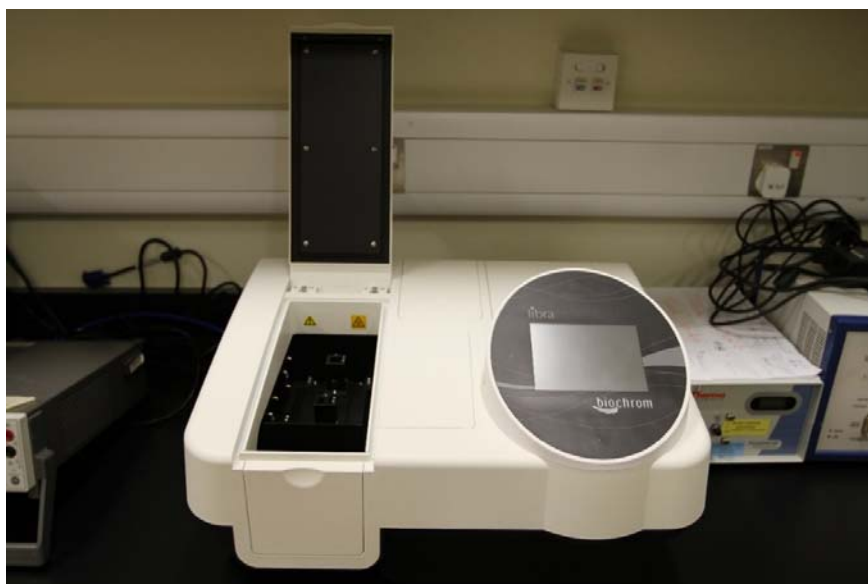


Figure 17. Ultraviolet/visible spectrophotometer, Biochrom Libra model S50.

CHAPTER 4: RESULTS AND DISCUSSIONS

This chapter introduces the physical and chemical analysis of the ZnO and Ag-doped ZnO nanomaterials. Followed by the detailed analysis of five PS nanocomposites (PS, PS/ZnO, PS/Ag-ZnO (1-3 wt.%)). Finally, we discuss the enhanced properties of the prepared nanocomposites and its morphological correlation to oil/water separation efficiency.

4.1 Structural characterization of nanomaterials

In this section, the structural analysis of ZnO and Ag-doped ZnO nanomaterials is explained.

4.1.1 X-Ray diffraction analysis

Figure 18 shows the XRD patterns of the unmodified and modified ZnO nanomaterials. The basis of the figure represents the characteristic patterns of the prepared ZnO and Ag in accordance to the database of the used instrument (PANalytical Empyrean diffractometer). This comparison led to the confirmation of the presence of the crystal structure for both prepared samples. The formation of the ZnO peaks are in accordance to JCPDS 36-1451, as the high intensity ranging from 30-40° belong to the (100), (002), and (102) planes. This confirms the common wurtzite structure, which is the standard crystal structure of ZnO [17, 100]. Additionally, Three new peaks were observed at 38.1°, 44.5° and 64.5°, which respectively correspond to the (111), (200), and (220) plane structure. These peaks suggest the presence of Ag in face centered cubic (FCC) crystal structure, however, the low intensity of these peaks can be attributed to the low cluster formation [92]. During the silver doping, the Ag ions are expected to reside within the grain boundaries of the ZnO nanomaterial rather than its lattice, as evident by the lack of peak shift in the XRD pattern of the Ag doped ZnO sample. This is in accordance with the observation made by Karunakaran and co-workers [101], whom also found multiple matching peaks, including the 200 peak of

face centered cubic phase of metallic Ag at $\sim 44^\circ$.

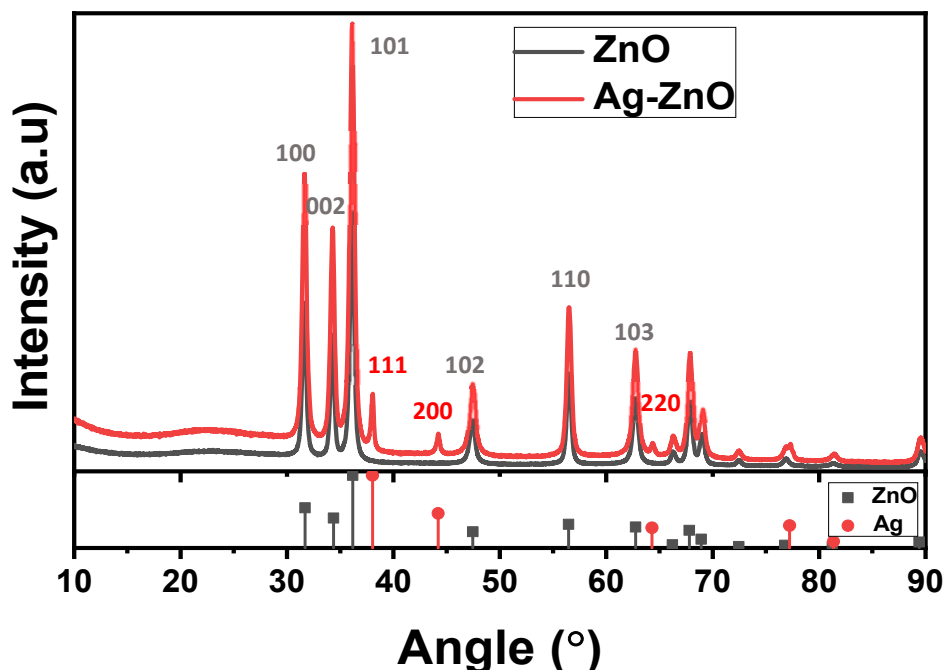


Figure 18. XRD pattern of ZnO and Ag-ZnO.

4.1.2 XPS analysis

XPS presents a good tool to analyse the content of the synthesized nanomaterial, through identifying its elemental composition. Figure 19 shows the XPS elemental analysis spectra with two symmetrical peaks at 1044.81 and 1021.64 eV belonging to Zn ($2p_{1/2}$) and Zn ($2p_{3/2}$) orbit coupling respectively. An important observation is the diversion of the recorded binding energy from the stoichiometric values of 1045.1 eV and 1022.1 eV, which is attributed to the charge transfer occurring between the zinc and oxygen ions. Figure 20 shows the oxygen spectrum with an asymmetric curve indicating two different types of atoms, the O^{2-} ions of ZnO bond and the one in the hydroxyl group [102]. Figure 21 shows binding energy for the silver. The results show two peaks at 368.3 eV and 374.3 eV attributed to Ag ($3d_{3/2}$) and Ag ($3d_{5/2}$). The binding energy difference of 6eV shows the presence of metallic silver in the Ag-ZnO sample. Since the electronegativity of Ag is higher than that of Zn, electrons are transferred from Zn to Ag, and this causes controlled defect formation in the ZnO lattice

[103].

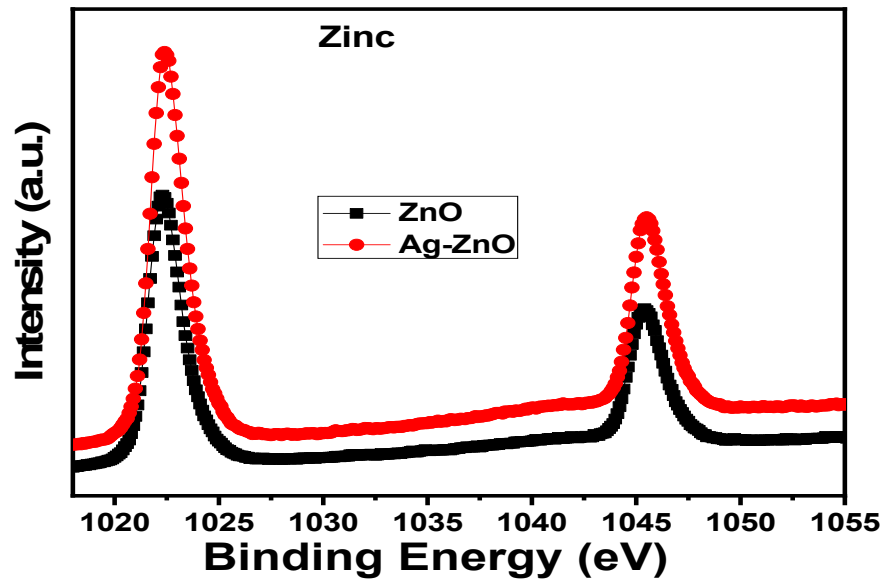


Figure 19. XPS spectra of ZnO and Ag-ZnO, with focus on zinc.

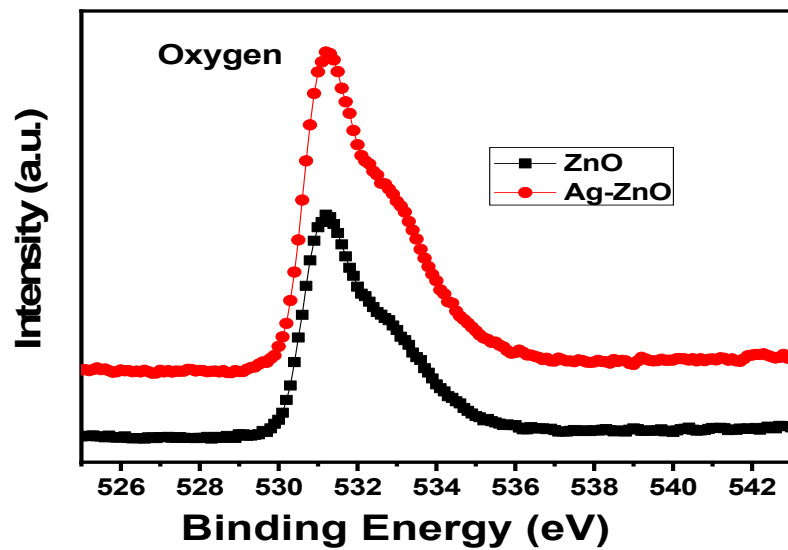


Figure 20. XPS spectra of ZnO and Ag-ZnO, with focus on oxygen.

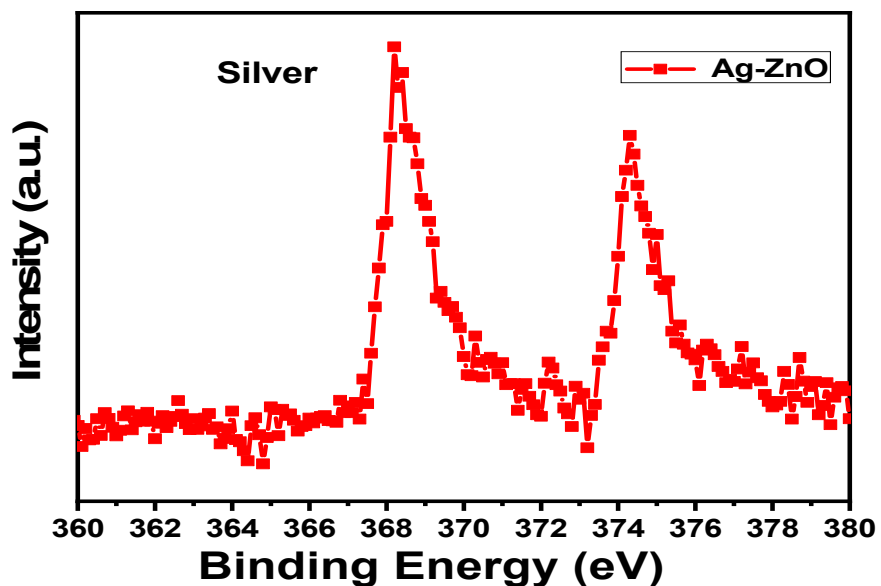


Figure 21. XPS spectra of ZnO and Ag-ZnO, with focus on silver.

4.1.3 FTIR analysis

Figure 22 represents the FTIR spectra of the ZnO and Ag-ZnO nanomaterial in the 500-4000 cm^{-1} range. Peaks near 500 cm^{-1} , 3300 cm^{-1} and 3000 cm^{-1} correspond to Zn-O stretching, -OH bending and the asymmetric and asymmetric C-H stretching vibrations respectively, similar to the results observed in the works of Hosseini et al. [104]. The absorption bands near 1000-500 cm^{-1} and at 1380 cm^{-1} can be attributed to the different vibrational influence of $-\text{CO}_3^{2-}$ group. When comparing the two spectra for both ZnO and Ag-ZnO, small shifts in peak positions are observed, this result is in agreement with Murtaza et al. [105] who studied the influence of Ag addition, concluding that the shift may be due to the partial Ag^+ substitution in the ZnO lattice. Moreover, no other prominent peaks are presented in both samples, indicating the phase

purity and confirming that the desired nanomaterials are prepared successfully.

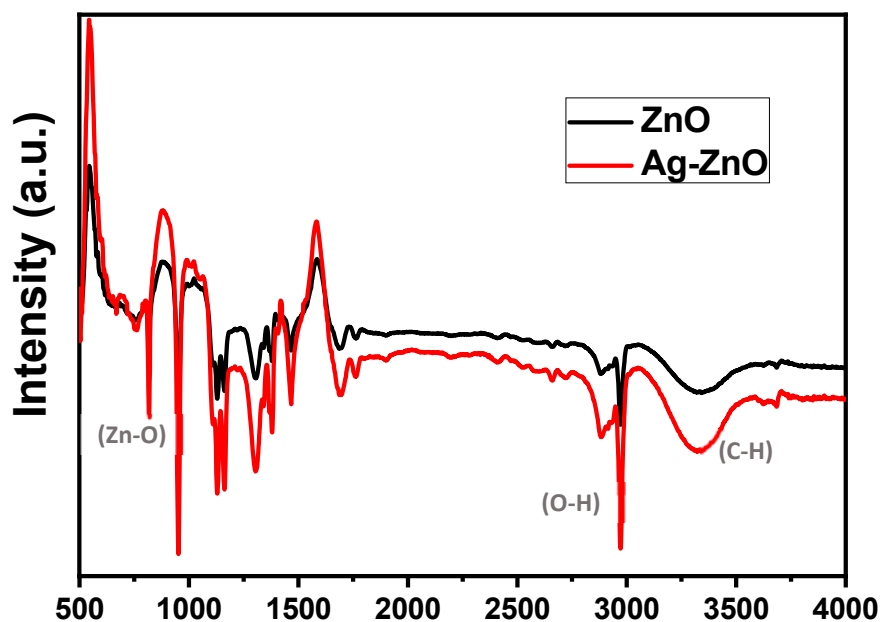


Figure 22. FT-IR curves of nano Ag-ZnO.

4.2 Structural characterization of nanocomposites

Structural analysis was done for the polymer and nanocomposites to ensure the degree of effectiveness in infusing both the nanomaterials dopant and polymer together. The modification of the PS polymer using ZnO and Ag-ZnO nanomaterials was characterized using XRD and FTIR techniques, to highlight the crystallinity and bond frequency change that occurs to the polymeric matrix once the inorganic dopant is introduced.

4.2.1 X-Ray diffraction analysis

The XRD results are shown in Figure 23. The small peaks that are visible at the 30-60° diffraction angle are presented due to the (100), (002), (101), (102) and (110) crystal planes of the ZnO [106]. These peaks are found to be prominent upon enhancing the Ag-ZnO concentration. The broad peaks observed around 10 and 18° correspond to the PS diffractions. The broadened peaks in the pure PS get narrower as the ZnO and

Ag doped ZnO concentration enhances. Moreover, a small peak shift is noticed as the concentrations of nanoparticles are increased. This is due to the formation of additional phase attributed to the nanoparticle distribution and the interphase generated by silver doping at the interstitial sites and ZnO lattice [107].

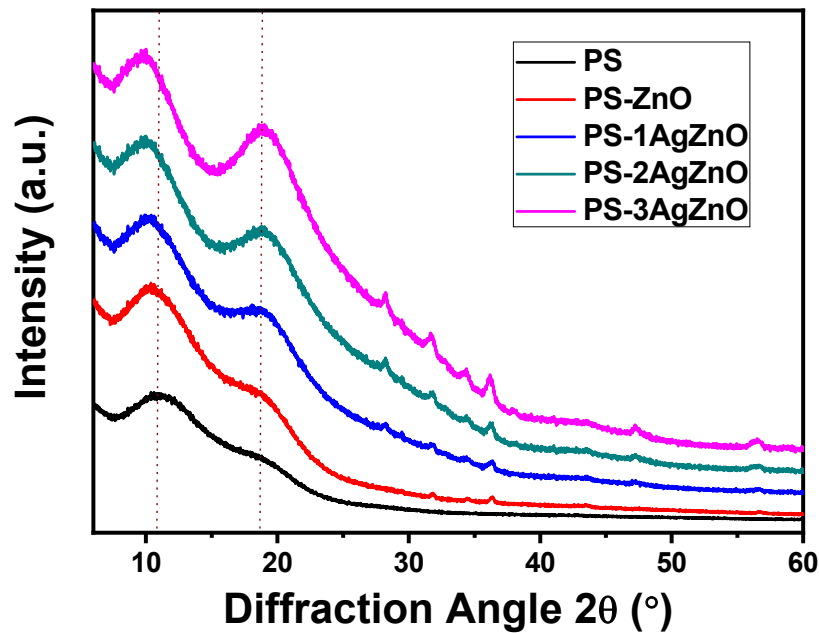


Figure 23. XRD pattern of pure PS and Ps/ZnO-Ag nanocomposite.

4.2.3 FTIR analysis

Figure 24 presents the FTIR spectra for all PS nanocomposites. The absorption peaks at 3027 and 2923 cm^{-1} correspond to aromatic C-H stretching. The vibrational peaks at 1454 cm^{-1} , 1491 cm^{-1} and 1602 cm^{-1} are due to the aromatic C=C bond stretching in styrene units, however the intensity change observed is due to the variation in nanoparticle concentration and its influence on the PS bond vibrations [107]. While the peak at 544 cm^{-1} corresponds to Zn-O bond vibrations, the peak at 695 cm^{-1} indicates the presence of styrene ring in all the composites [108]. The sharpening of the peaks and enhancement in intensity with increasing the filler concentration are indications of

PS/ZnO or Ag-ZnO interactions and might be due to better nano reinforcements in the composites [109].

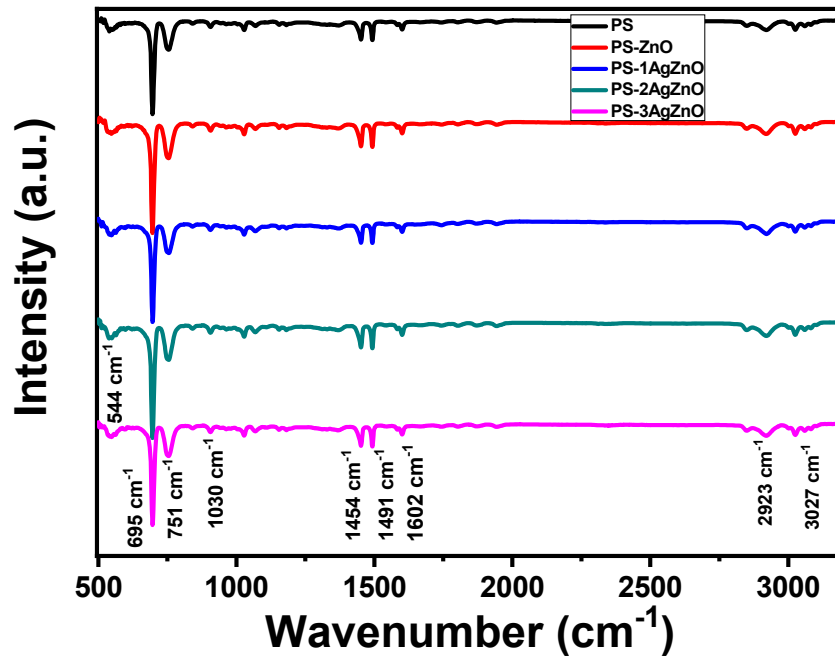


Figure 24. FT-IR curves of PS and PS/Ag-ZnO nanocomposites.

4.3 Morphological characterization of nanomaterials and polymer composites

4.3.1 SEM/TEM imaging of ZnO and Ag/ZnO nanomaterials

SEM and TEM as represented in Figure 25 addressed morphology of the nanomaterials. It is clear from the figure that silver doping causes no change in the spherical shape of the particles but changes the size and dimension of ZnO. Both SEM and TEM clearly illustrate the decrease in dimension of the particles after Ag doping. More clearly, the average particle size of ~ 50 nm for the ZnO was reduced to ~ 30 nm in the case of Ag-ZnO as seen in the inset of Figure 25 c and d. This supports the decrease in crystallite size observed from the XRD and thus the interstitial silver occupancy. In addition, the lattice spacing's were also calculated as demonstrated in the insets of Figure 25c and 25d. For the ZnO, the spacing was 0.80 nm whereas in the

case of Ag-ZnO, it increased to 0.95 nm. This also confirms the increase in lattice size upon silver doping [60]. Hence the structural and morphological analysis are in good agreement, confirming the expansion of ZnO crystal lattice and the substitution of Ag⁺ ions [110].

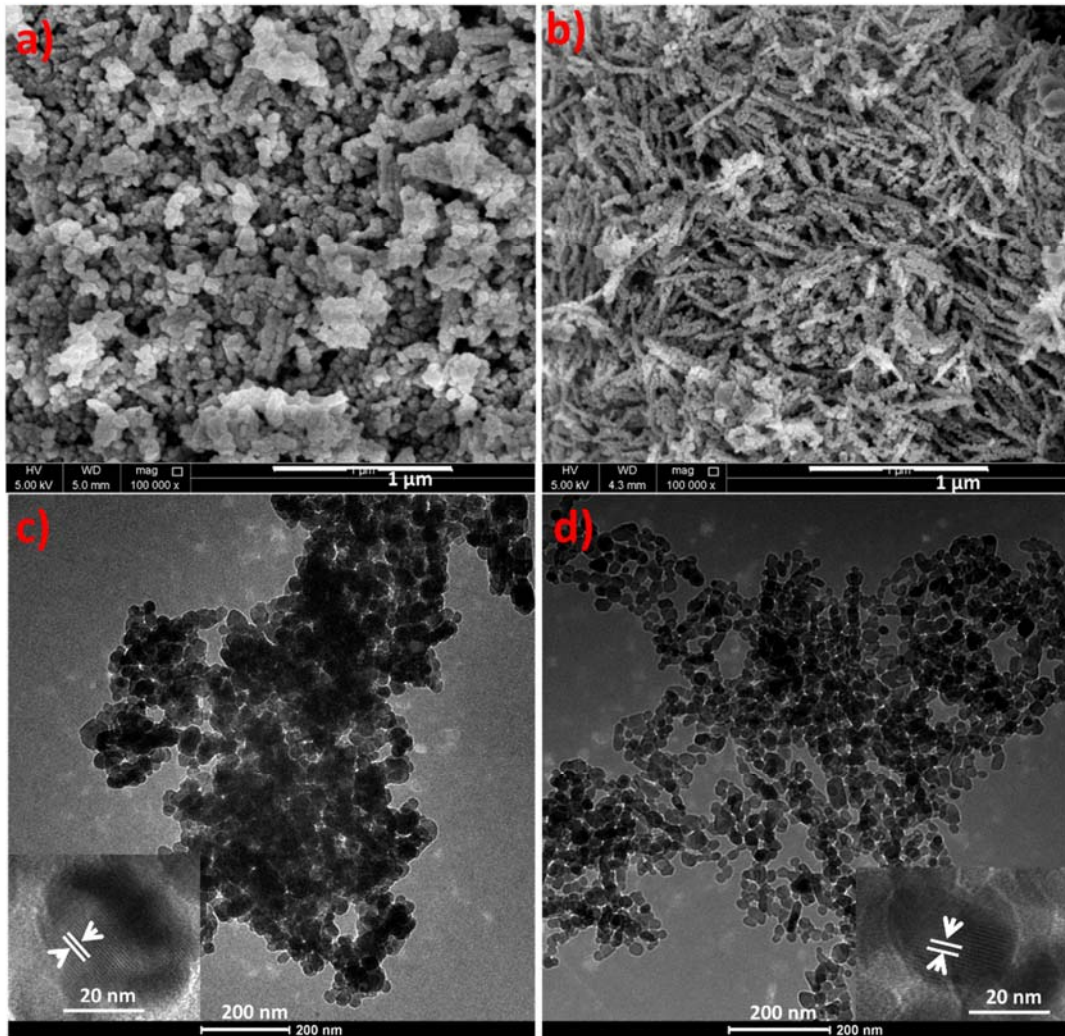


Figure 25. SEM images of a) ZnO and b) Ag-ZnO; TEM images of c) ZnO and d) Ag-ZnO..

4.3.2 SEM/TEM imaging of PS and PS nanocomposites

Morphology of the nanofibers were investigated using the SEM (Figure 26). The porous nature of the fibers are clearly observed. The pores formation on the surface of all fibers is mainly due to the non-solvent induced phase separation mechanism [111]. During the synthesis process, the PS undergoes phase separation as the non-

solvent penetrates to the polymer structure. As this happens, electrospinning evaporates the solvent and decreases the surface temperature. During the solidification process, the composition reverts to its phase separation form, thus the porous structure is created. The average pore size as seen in Figure 26 inset is 189 nm, 113 nm, 171 nm, 145 nm, 96 nm for PS, 2wt.% PS/ZnO, 1wt.% PS/Ag- ZnO, 2wt.% PS/ Ag- ZnO, and 3wt.% PS/Ag- ZnO fibers respectively. The pores concentration increases with an increase in the nanoparticle concentration, while the fiber diameter decreases. This is observed in Figure 26 inset, hence the 3wt.% PS/Ag- ZnO fibers has an average of 500 nanopores ranging from 0 to 100 nm, in comparison to the neat PS fiber which has an average of 100 nanopores ranging from 0 to 100 nm.

This again confirms the nanoparticle polymer interfacial interaction and influence of Ag-ZnO in fiber and pore formation, as the increase in pores distribution seems to be directly linked to the increase in nanomaterials concentration within the fiber. Similar behaviour was noticed by Ponnamma et al. through the electrospinning of PVDF containing Fe doped ZnO nanomaterials. The increase in nanoparticle incorporation led to the decrease in the fibers diameter, as the overall tension in the fiber is dependent on the self-repulsion which is induced through excess charges on the electrospun jet [112, 113]. Therefore, the addition of Ag doped ZnO nanoparticles led to the build up of higher charge density on the surface of the emitted jet and increased the overall electric charge of the electrospun polymer composite. The increase in carried charges caused higher elongation forces that could overcome the sel-repulsion force. Thus leading to the assumption that an increase in carried charges leads to a higher rate

of evaporation which causes an increase in porosity and a decrease in the diameter [114, 115].

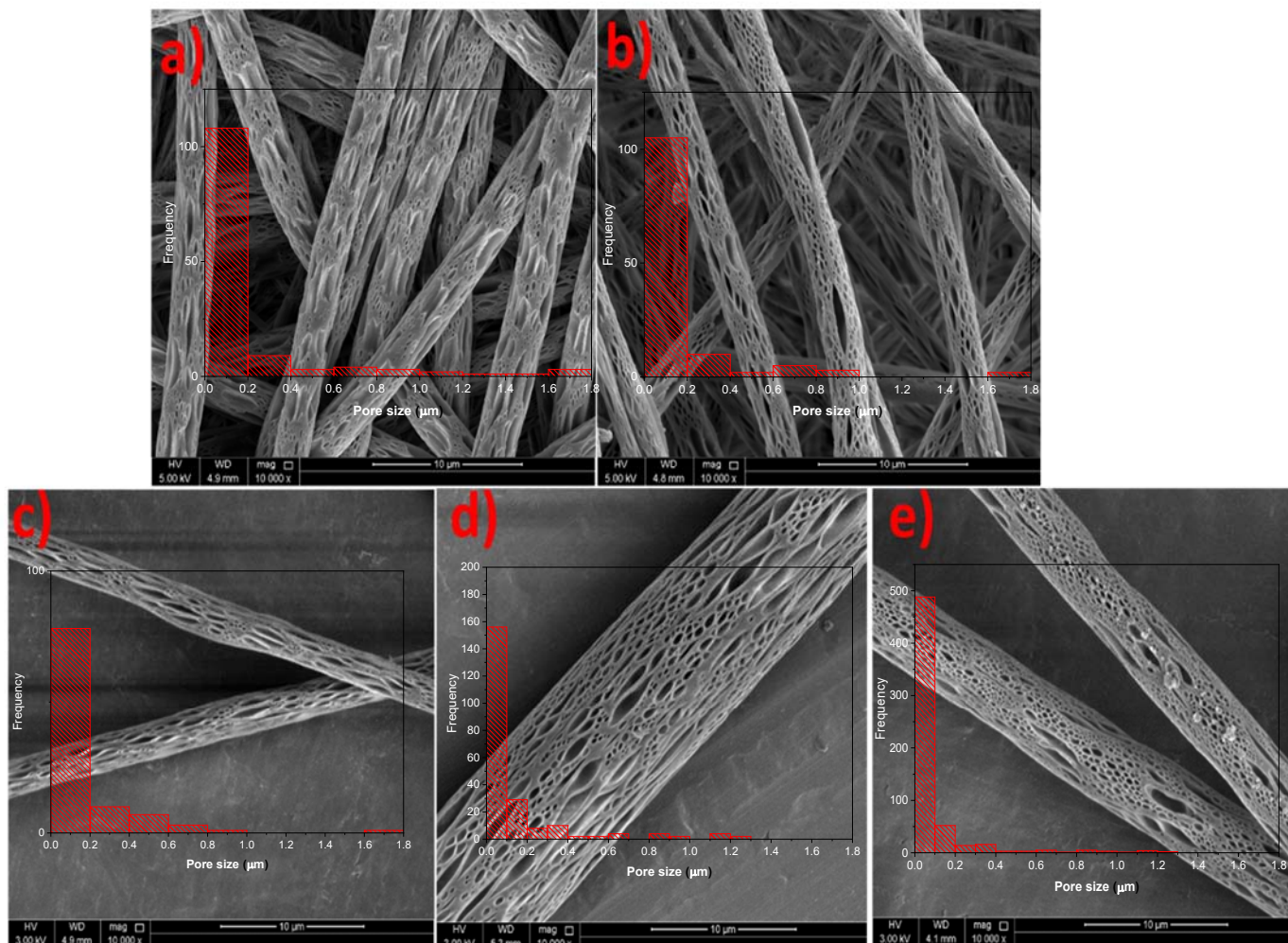


Figure 26. SEM images for the a) PS and PS nanocomposites b) with 2 wt.% ZnO, c) with 1 wt.% Ag-ZnO d) with 2 wt.% Ag-ZnO and e) 3 wt.% Ag-ZnO

4.3.3 EDX analysis

Figure 27 shows the dispersion of the nanoparticles within the PS based nanocomposites. Both 2wt.% PS/ZnO and 2wt.% PS/ZnO-Ag samples were analyzed for the elements distribution. As shown in Figure 27, the corresponding Zn and Ag elements are presented uniformly in respective samples. The effectiveness and application of the prepared fibers relies heavily on the uniform distribution of the

nanomaterials, in order to maximize desired properties of the nanomaterials, including increase in porosity and anti-bacterial effect. Furthermore, increase in distribution of nanomaterials in the polymer can increase chemical, thermal, and physical properties of the matrix [116]. The EDX images clearly explain the well distribution of the nanoparticles within the nanocomposites [117, 118]. This uniform particle distribution in the PS fibers can influence the fiber porosity as well. As mentioned earlier in this

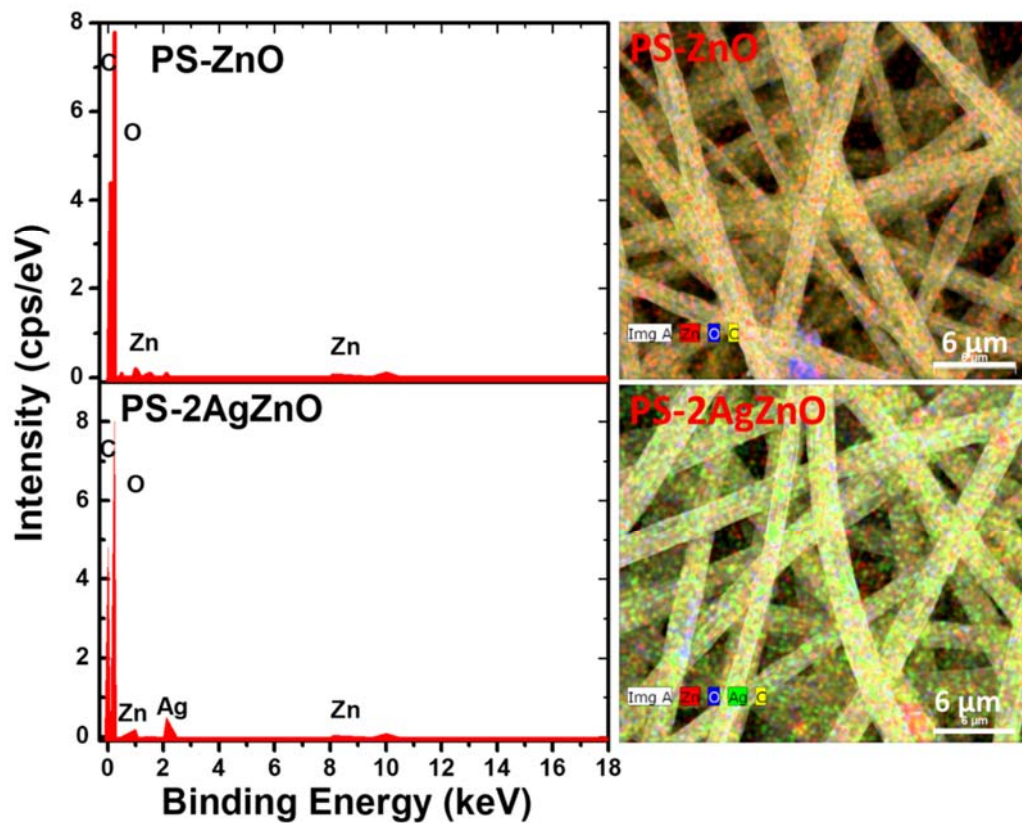


Figure 27. Energy dispersive spectra and EDX images for 2wt.% PS/ZnO and 2wt.% PS/ZnO-Ag nanocomposites.

chapter, it is perceived that the increase in the nanomaterials concentration within the fibers leads to an increase in the carried charge, causing a networking effect within the polymer chains, therefore affecting the elongation time, which allows the fibers to form an elongated version with higher pores distribution in comparison to pure PS fibers.

4.4 Mechanical stability of the polymer nanocomposite

Mechanical stability is a very important characteristic for oil separation membranes' efficiency, as it should withstand high water flux. Table 5 represents the mechanical strength in terms of Young's modulus, tensile strength and elongation at break for the PS and its nanocomposites. It is clear from the values that the mechanical properties are enhanced with nanomaterials addition [119, 120]. With the Ag-ZnO at 2 wt.%, the neat PS increased its Young's modulus and tensile strength by 2.4 times. However, the nanomaterials do possess a leveling effect after a specific concentration, which is often correlated with the agglomeration issues at higher weight percentages [121, 122]. In our case, the optimum filler concentration is identified as 2 wt.% of Ag-ZnO. It is also noticeable that the insertion of Ag nanoparticles led to the increase in young's modulus and the percentage of elongation at break in comparison to PS and PS/ZnO samples. This can be attributed to the increase in the toughening level attributed to the presence of Ag nanoparticles, as the inclusion of Ag nanoparticles is known for its increase in interfacial fracture resistance and networking effect through its occupation of the interstitial sites of ZnO [123].

Table 5. Mechanical properties of the PS and its nanocomposites containing ZnO and Ag-ZnO.

Samples	Tensile Strength (MPa)	Young's Modulus (MPa)	Elongation at break (%)
PS	1.20 ± 0.11	13.45 ± 0.33	43.0 ± 2.15
PS-ZnO	2.15 ± 0.56	15.75 ± 0.25	40.5 ± 2.80
PS-1AgZnO	1.84 ± 0.53	20.84 ± 0.43	42.5 ± 0.95
PS-2AgZnO	2.77 ± 0.16	36.56 ± 0.92	39.5 ± 0.50
PS-3AgZnO	2.52 ± 0.45	34.11 ± 0.85	38.9 ± 2.50

4.5 Thermal stability of the polymer nanocomposite

The thermal stability of the PS nanocomposites is illustrated in Figure 28. It is clear from both the thermograms and derivative thermograms that the nanoparticles enhanced the degradation temperature of PS and thus the thermal stability. While pure PS decomposes at 415.3°, the nanocomposite containing 2 wt.% Ag-ZnO decomposes at 419.9°. The inset of the figure marks the onset of degradation temperature, which also shows the higher thermal stability for the composite containing 2 wt.% of Ag-ZnO. The Ag doped ZnO offered better dispersion and improved the interfacial interaction with PS, compared to ZnO. This is due to the combined heat resistance property of Ag and ZnO as an inorganic thermal retardant. This result is in agreement with the findings of Ma et al. [109], where they also noticed an increased thermal stability while increasing the ZnO % in a PS resin nanocomposite [111]. However, at higher percentages, the possible agglomerations within the polymer medium may cause loss of thermal stability due to the reduction in the contact surface between the nanomaterials and the polymer matrix.

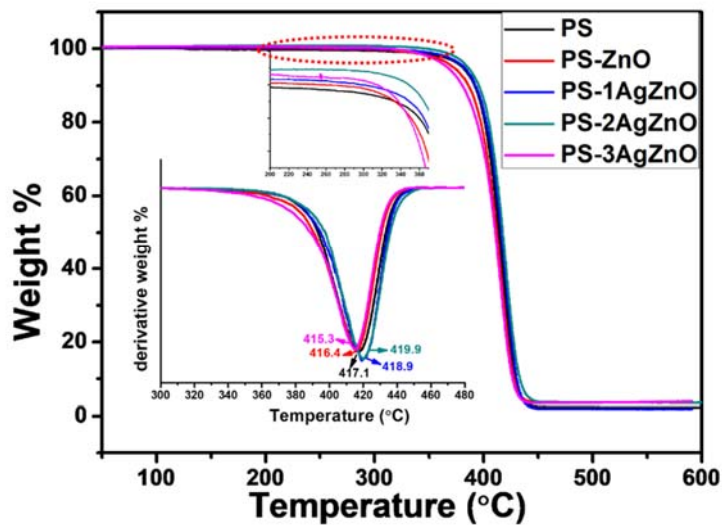


Figure 28. TGA curves for the PS and its nanocomposites; inset shows the onset of degradation and the derivative thermograms.

4.6 Wettability of the PS and PS/Ag-ZnO nanocomposite

The surface hydrophilicity/hydrophobicity is an important property for oil/water separation systems, as the selectivity of oil absorption is a crucial property in the separating process. The electrospun fibers are tested for their water contact angle. The values are represented in Figure 29, in which the hydrophobicity increase can be clearly observed. As the nanoparticles are added to the PS medium, the contact angle value increased from 122.3° (pure PS) to a maximum of 136.1° with (3wt.% Ag-ZnO). This can be attributed to the improvement in encapsulation efficiency of the nanomaterials within a polymeric medium, in addition to the increase in surface roughness on the nanoscale level, which is correlated with increase in surface area provided by the nanomaterial inclusion [124-126]. The composite containing the 2 wt.% of Ag-ZnO possesses a contact angle value of 135.9° indicating the levelling effect of the surface hydrophobicity after 2 wt.%. This result is in good agreement with the structural and morphological properties of the nanocomposites which clearly indicated the optimum Ag-ZnO concentration as 2 wt. %. Surface porosity induced by the non-solvent induced phase separation process is also responsible for the higher contact angle in addition to the nanoparticle addition. Other researchers have also observed successful increase in hydrophobicity through the increase of the nanomaterial content in the polymeric substrate, including Radwan et al. where the hydrophobicity of the PVDF increased due to the addition of ZnO. This increase was mainly due to the increasing air entrapment within the surface interface [127].

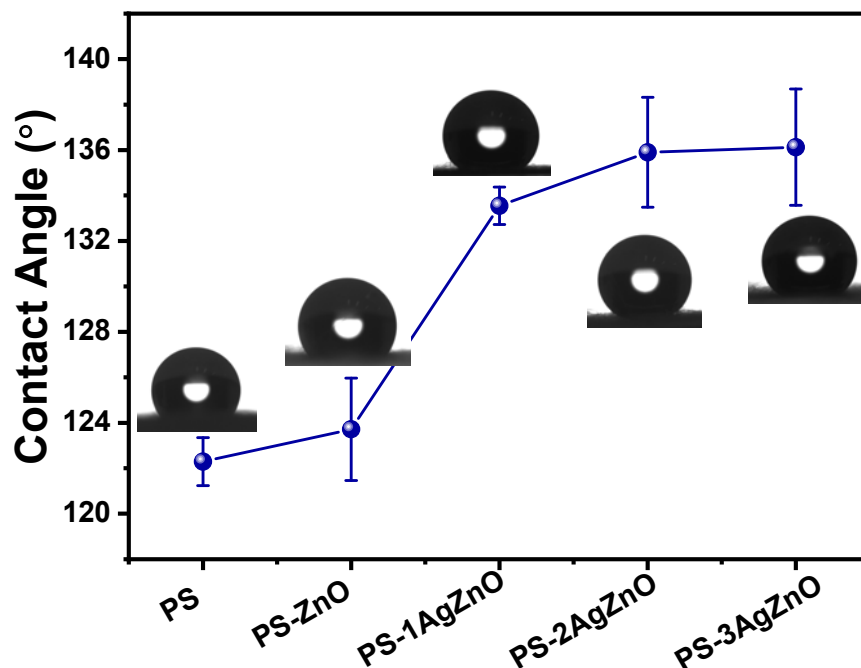


Figure 29. Water contact angle values for the PS and PS nanocomposites.

4.7 Maximum oil absorption capacity of PS and PS/Ag-ZnO nanocomposite

Oil absorption capability of the PS nanocomposites were studied using three different oils: engine oil, olive oil and mineral oil. The average oil absorption capacities obtained for all samples are illustrated in Figure 30. The oil absorption varies with various parameters such as viscosity of the oil, amount/area of the fiber, immersion time etc. In this case, the amount of the nanocomposite (10 mg), and absorption period were kept uniform and the main factors affecting the absorption performance was limited to the nature of the nanocomposite and the nature of the oil. In all cases, the oil absorption increased with the increase in nanomaterials concentration within the PS polymer, this is largely due to the increase in porosity found in the fibers. It is clear from the SEM studies that the concentration of nanomaterials led to an increase in pores distribution within the fiber. This allowed for enhanced absorption within highly concentrated PS/Ag-ZnO sample in comparison to the PS and PS/ZnO samples. Upon

comparing the oils, the density and viscosity are the prime factors regulating the performance. The density of olive oil (0.924 g/ml) was the highest and that of mineral oil (0.869 g/ml) the least. However, the viscosity values of the oils followed the following trend engine oil (496 mPas) > mineral oil (154 mPas) > olive oil (68.6 mPas). Moreover, the surface tension values of the oils were also measured with respective values of 35, 33 and 32 mN/m for the olive, engine and mineral oils respectively. These results point towards the combined influence of density, viscosity and surface tension of oils on the relative absorption performance of the fibers. Thus the polymer nanocomposite can be tailored to the required absorption of oil type and the achieved

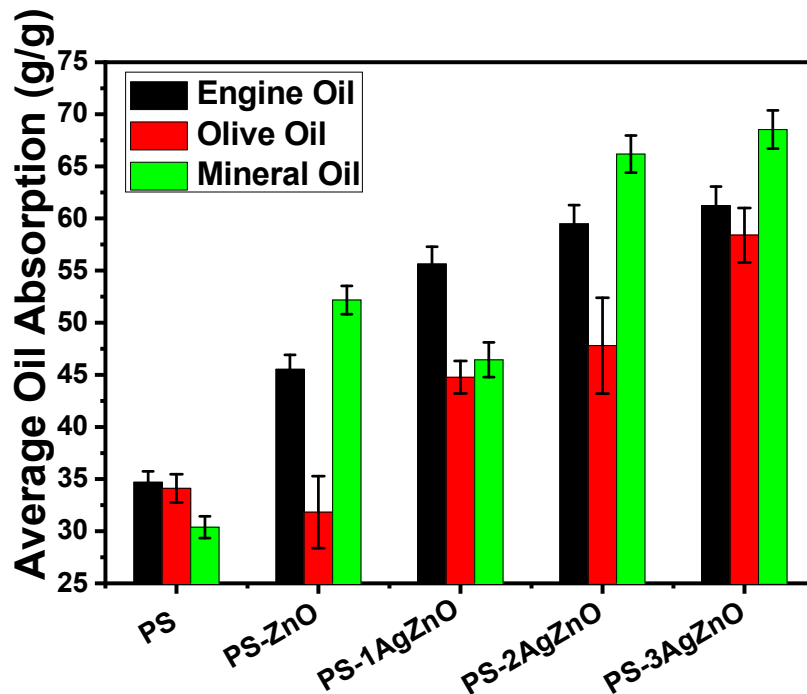


Figure 30. Oil absorption values for the PS and PS nanocomposites.

enhancement in the absorption efficiency [128]. Other comparative works showed significantly less oil absorption capacity, which were summarized in chapter 2 table 3. Co-axial electrospun PS/polyurethane fibers were reported as a similar system with value of 64.40 g/g of motor oil [129].

4.8 Recyclability of the 2 wt.% of PS/Ag-ZnO nanocomposite

The durability of the membrane is a prime parameter for possible material application. In order to test the industrial usage, clean-ability and reusability of the fibers were tested, and the obtained results are compared in Figure 31. Oil/water separation efficiency of the best polymer nanocomposite (2 wt.% of Ag-ZnO) (were tested using the laboratory set up mentioned in 3.3.9. The separated water in Figure 31 is compared with the preliminary oil/water mixture in terms of total organic content (TOC). It is found that the TOC value for the oil/water emulsion was decreased from 194.74 ± 0.35 to 155.49 ± 0.5 in separated water, after the first cycle of oil/water separation. It is clear from the inset of Figure 32a and 32b that, the oil molecules are absorbed within the fibers pores. This is a good evidence for the oil removal efficiency of the porous nanocomposite fibers. The repeatability of oil/water separation is shown in Figure 31, the same oil/water emulsion sample was filtered continuously for up to 5 cycles. It is found that the efficiency of separation increases upto cycle 4, however, at cycle 5 the sample reached its maximum oil absorption saturation.

As represented in Figure 32a (Pure PS) and 32b (2 wt.% of Ag-ZnO), the oil wets the fibers during oil/water separation. The pores on the fibers were covered with

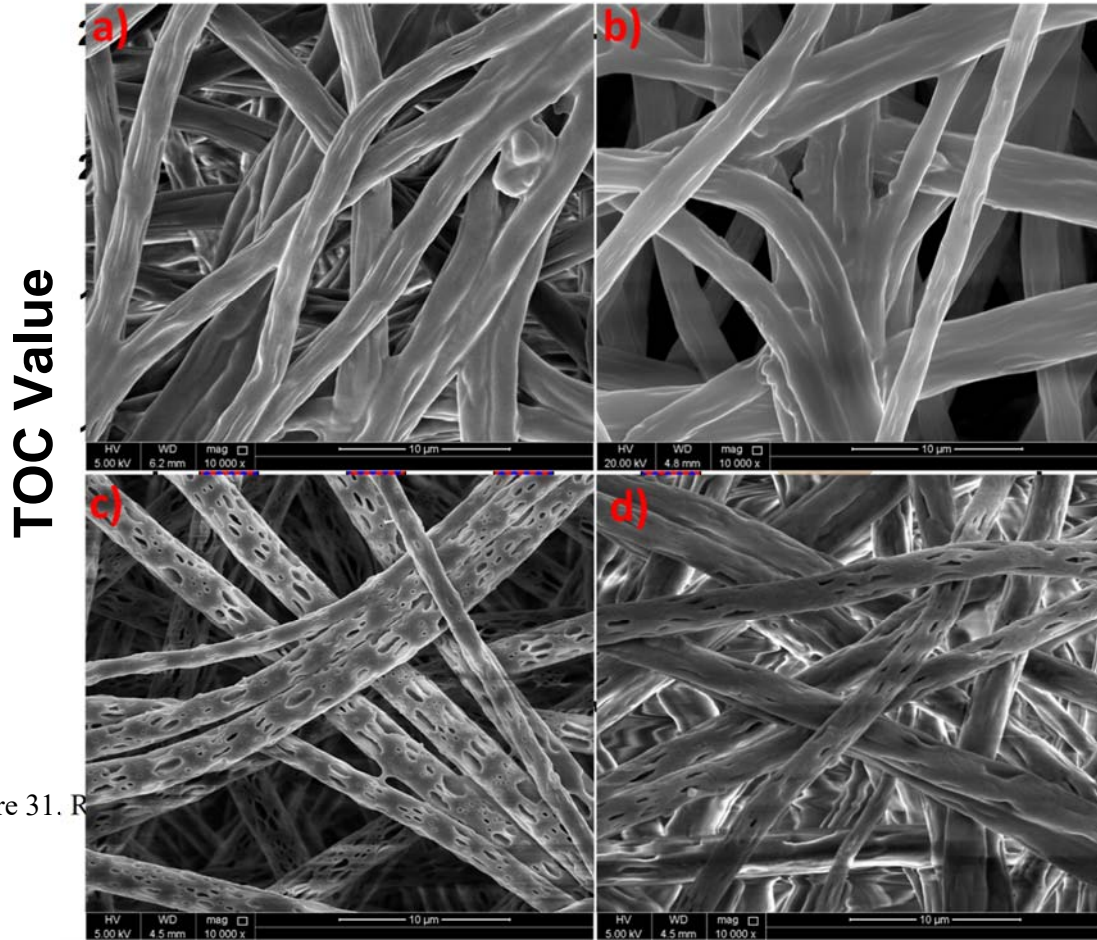


Figure 31. R

ycles.

oil, as they are not visible in the figures. Utilizing NaOH as a cleaning surfactant

Figure 32. SEM images of a) PS and b) 2 wt.% of Ag-ZnO wetted in oil; c) PS and d)

2 wt.% of Ag-ZnO washed with NaOH.

enables the fibers to reacquire their porous structure (Figure 32c for pure PS and 32d for 2 wt.% of Ag-ZnO), however comparison with the original SEM images of the fibers in Figure 26, confirms the reduced pore size and fiber flexibility. The fibers were tested for 4 cycles and the results were consistent.

4.9 Antifouling capability of PS and PS/Ag-ZnO nanocomposite

Biofouling or formation of hard to remove bacterial films on the surface of the material, is a serious problem affecting the durability of the membranes used for oil water separation. The antibacterial property of the 2 wt.% of Ag-ZnO fibers (Figure 33b) is compared against the control (Figure 33a) as indicated. The neat PS itself has higher antibacterial property [130], which is further enhanced by the presence of silver doped ZnO nanomaterials [131]. This substantiates the possibility of the tailored materials usage in oil/water separating applications, due to no bacterial agglomeration. This is expected with the modified ZnOAg nanocomposite, as Ag is known for its antibacterial behavior.

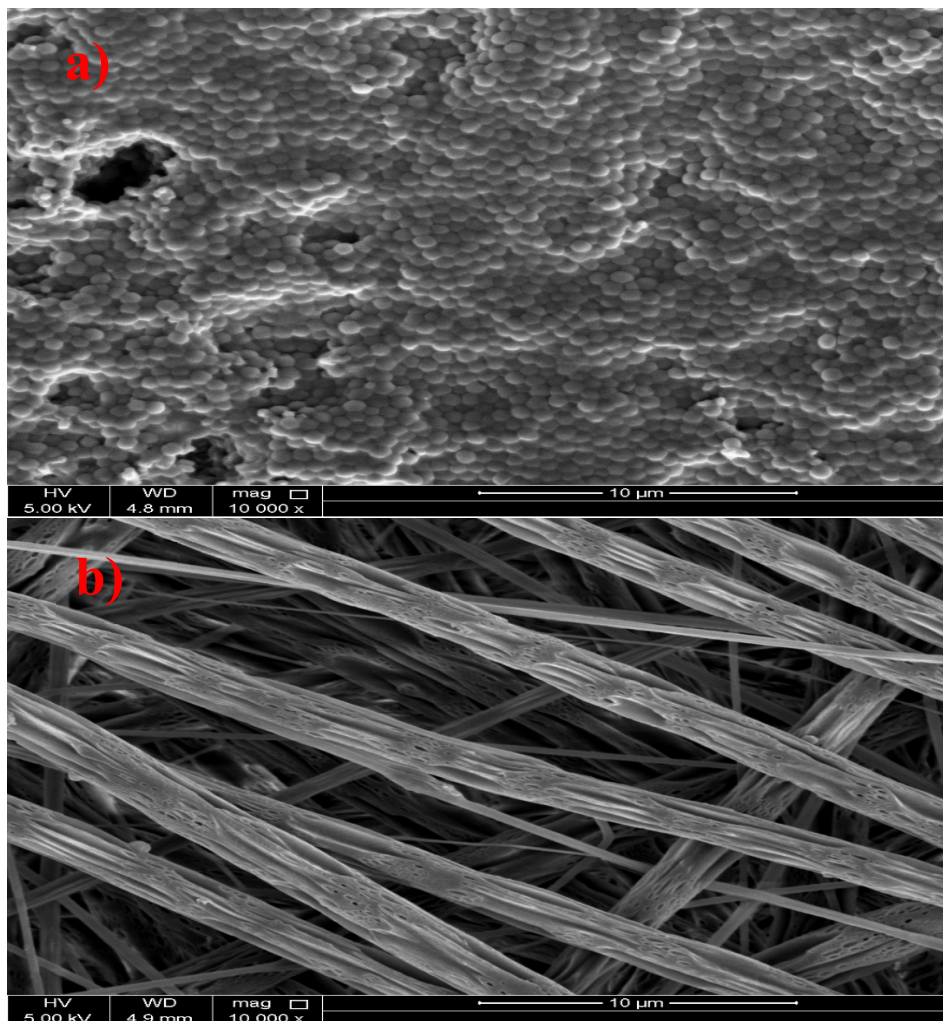
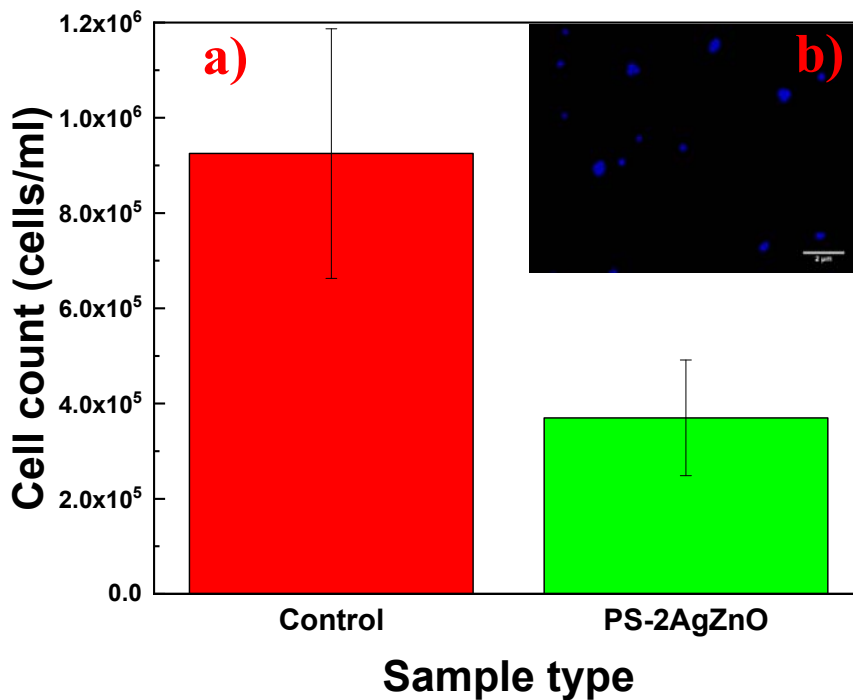


Figure 33. a) control, b) 2 wt.% of Ag-ZnO after bacterial growth. Inset shows the bacteria grown samples.

The bacterial quantification experiment was done in 3 independent biological replicates, through collecting stained bacterial suspension and manually counting the bacteria produced. 2-tailed Student's t-test was applied on the 3 data points. p-value of less than 0.05 was considered statistically significant. As seen in figure 34 a, the bacterial concentration of *S. aureus* was much lower in the polymer nanocomposite sample (3.7×10^5 cells/ml) in comparison to the control (9.25×10^5 cells/ml). The reason behind the low bacterial concentration of PS-2AgZnO fibers is due to their ability to suppress the migration of the bacteria through the membrane, which is in agreement with SEM imaging found in figure 33 a) and b). In addition to the high antibacterial activity of silver nanoparticles, which stems from the free radical generation produced



by Ag metals and ions which are extremely toxic to microorganisms [132, 133].

Figure 34. a) bacterial cells grown on control filter and PS/2% Ag-ZnO, b) example of stained bacteria under 60x magnification.

4.10 Photodegradation capability of PS/Ag-ZnO nanocomposite

The produced polymer nanocomposite can have another role in water industry, which is limiting the presence of toxic organic compounds in water through photodegradation. The photodegradation property of 2 wt.% Ag-ZnO polymer nanocomposite (Figure 35 a)) demonstrates the capability of the polymer nanocomposite to reduce the concentration of common organic test dye rosindulin (azocramine G dye) in water through the concentration change recorded at 528 nm. The double sulfonated water-soluble red dye clearly started to lose its color after the 3H/4H mark, signaling the degradation of the organic structure of rosindulin as seen in figure 35 inset. This process was initiated through solar irradiation which excites the Ag doped ZnO into forming an electron-hole pair, allowing the electron to migrate to the nanomaterials surface and react with water to form OH radicals [134], causing a chain of reaction between the produced radicals and the rosindulin dye. The rosindulin dye has a maximum absorbance at 528 nm, matching the maximum absorbance found in literature [135]. Figure 35 b demonstrates the degradation of the dye concentration to around 10% after 6 hours of exposure to solar irradiation. The predicted mechanism of rosindulin degradation according to Divband et al. [136] starts with solar irradiation forming an electron/hole pair in ZnO and Ag, which then reacts with O₂ and H₂O molecules to form OH[•] radicals, the following radicals then degrade the rosindulin dye through oxidation, and the formation of non-toxic fragments.

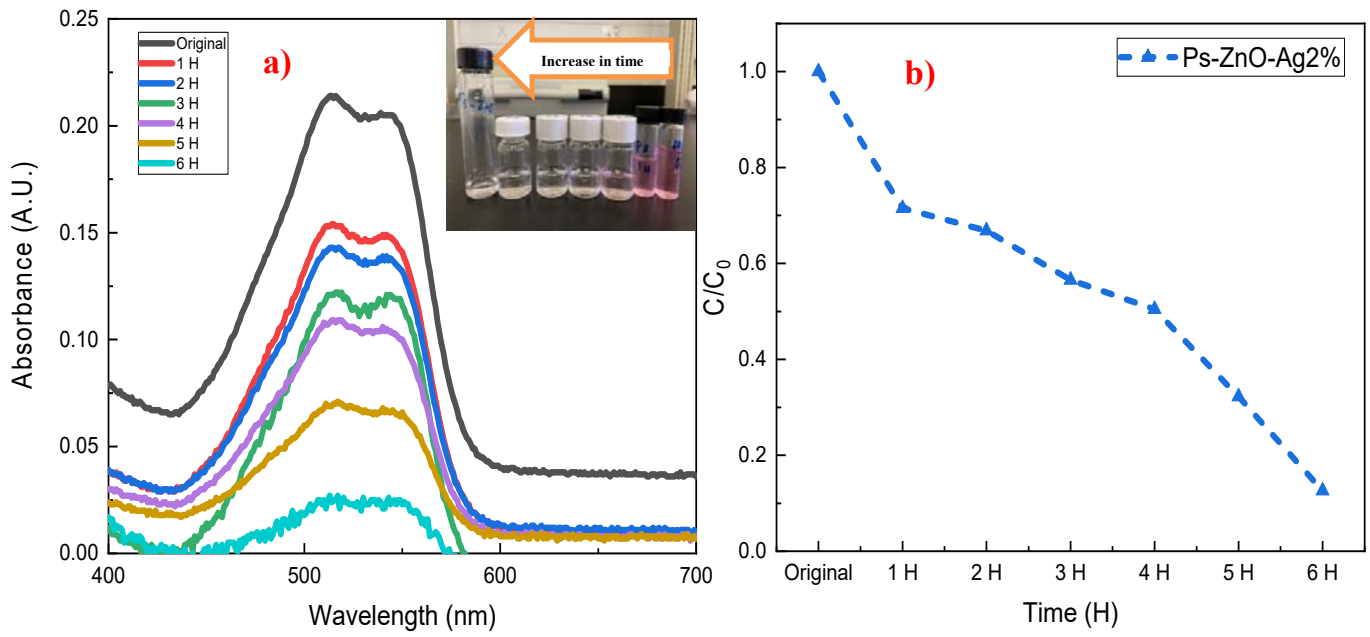


Figure 35. a) The concentration changes of rosindulin at 528 nm in presence of 2 wt.% Ag-ZnO b) The change in concentration of rosindulin solution in the presence of 2 wt.% Ag-ZnO.

CHAPTER 5: CONCLUSION

In the current study, novel tailored porous nanocomposite were investigated. The separation efficiency of the prepared samples exhibited a successful 62% total organic concentration reduction. The chemical, physical and mechanical properties of these samples were characterized, and the major research findings from this study can be summarized as follows:

- During the nanomaterial synthesis, Ag ions were doped to the ZnO lattice with modification on its structural property, and the amount of silver ions was enough to significantly improve the polymers properties.
- Novel approach in producing doped porous fibers using non solvent induced phase separation mechanism, which was the reason to form porous fibers during electrospinning. Leading to enhanced surface roughness of the fibers, due to both the fabrication method and the nanoparticle addition, which is quantified through the increase in contact angle from 124 to 136 °.
- Uniformly distributed Ag-ZnO nanomaterials increases the porosity of the fiber, leading to higher frequency of pores within the nano range. This increases possibility of absorbing oil, with a maximum absorption capacity of 68.54 g/g for mineral oil.
- The tensile strength and Young's modulus of the prepared polymer nanocomposite is up to 2.4 times higher in comparison to neat PS.
- The optimum nanomaterial doping concentration was found to be at 2 wt.% Ag-ZnO, hence the 2 wt.% polymer nanocomposite sample possessed the best chemical, mechanical, hydrophobic, and oil retaining properties.

FUTURE WORK

A one-step porous nanocomposite fibers were produced for possible oil/water separation, with clear physical and chemical property elevation. This nanocomposite had high value of oil retainability, therefore its utilization in disposing of oil contaminants in oil spills or industrial wastewater is clear. The novelty emerges from the ability to reuse and recycle the sorbent to ensure minimal environmental waste. Therefore, the future works aims to fabricate PS nanocomposites with further enhanced properties, such as more oil/water emulsion separation cycles, maximum oil absorption from industrially contaminated water streams, and better compatibility between the nanocomposite and currently used commercial membrane to increase their antifouling capabilities.

References

1. Koo, J.H., *Polymer nanocomposites*. 2006: McGraw-Hill Professional Pub.
2. Jordan, J., et al., *Experimental trends in polymer nanocomposites—a review*. *Materials science and engineering: A*, 2005. **393**(1-2): p. 1-11.
3. Gausepohl, H. and N. Nießner, *Polystyrene and Styrene Copolymers em: “Encyclopedia of Materials: Science and Technology”*. Buschow KHJ, Cahn RW, Flemings MC, Ilshner B, Kramer EJ, Mahajan S. Elsevier, Amsterdam, 2001. **8**: p. 7735.
4. Neinhuis, C. and W. Barthlott, *Characterization and distribution of water-repellent, self-cleaning plant surfaces*. *Annals of botany*, 1997. **79**(6): p. 667-677.
5. Tuteja, A., et al., *Designing superoleophobic surfaces*. *Science*, 2007. **318**(5856): p. 1618-1622.
6. Lathe, S.S., et al., *Sliding behavior of water drops on sol-gel derived hydrophobic silica films*. *Applied Surface Science*, 2010. **256**(10): p. 3259-3264.
7. Dhere, S.L., et al., *Transparent water repellent silica films by sol-gel process*. *Applied Surface Science*, 2010. **256**(11): p. 3624-3629.
8. Afzaal, M., M.A. Malik, and P. O’Brien, *Preparation of zinc containing materials*. *New Journal of Chemistry*, 2007. **31**(12): p. 2029-2040.
9. Mills, A. and J. Wang, *Simultaneous monitoring of the destruction of stearic acid and generation of carbon dioxide by self-cleaning semiconductor photocatalytic films*. *Journal of Photochemistry and Photobiology A: Chemistry*, 2006. **182**(2): p. 181-186.
10. Norton, D.P., et al., *ZnO: growth, doping & processing*. *Materials today*, 2004.

- 7(6): p. 34-40.
11. Tarwal, N. and P. Patil, *Enhanced photoelectrochemical performance of Ag-ZnO thin films synthesized by spray pyrolysis technique*. *Electrochimica Acta*, 2011. **56**(18): p. 6510-6516.
 12. Gouvêa, C.A., et al., *Semiconductor-assisted photodegradation of lignin, dye, and kraft effluent by Ag-doped ZnO*. *Chemosphere*, 2000. **40**(4): p. 427-432.
 13. Akhavan, O. and E. Ghaderi, *Enhancement of antibacterial properties of Ag nanorods by electric field*. *Science and technology of advanced materials*, 2009. **10**(1): p. 015003.
 14. Chen, P.-Y. and S.-H. Tung, *One-Step Electrospinning To Produce Nonsolvent-Induced Macroporous Fibers with Ultrahigh Oil Adsorption Capability*. *Macromolecules*, 2017. **50**(6): p. 2528-2534.
 15. Yudin, V., et al., *New polyimide nanocomposites based on silicate type nanotubes: Dispersion, processing and properties*. *Polymer*, 2007. **48**(5): p. 1306-1315.
 16. Ma, P.-C., et al., *Dispersion and functionalization of carbon nanotubes for polymer-based nanocomposites: a review*. *Composites Part A: Applied Science and Manufacturing*, 2010. **41**(10): p. 1345-1367.
 17. Georgekutty, R., M.K. Seery, and S.C. Pillai, *A highly efficient Ag-ZnO photocatalyst: synthesis, properties, and mechanism*. *The Journal of Physical Chemistry C*, 2008. **112**(35): p. 13563-13570.
 18. Parangusan, H., D. Ponnamma, and M.A.A. Al-Maadeed, *Stretchable electrospun PVDF-HFP/Co-ZnO nanofibers as piezoelectric nanogenerators*. *Scientific reports*, 2018. **8**(1): p. 754.
 19. ISO, T., *80004-4 Nanotechnologies–Vocabulary–Part 4: Nanostructured*

- Materials*. ISO, Geneva, 2011.
20. Schmid, M., et al., *Fundamental investigations regarding barrier properties of grafted PVOH layers*. International Journal of Polymer Science, 2012. **2012**.
 21. Schmid, M., et al., *Water repellence and oxygen and water vapor barrier of PVOH-coated substrates before and after surface esterification*. Polymers, 2014. **6**(11): p. 2764-2783.
 22. Okada, A. and A. Usuki, *Twenty years of polymer-clay nanocomposites*. Macromolecular materials and Engineering, 2006. **291**(12): p. 1449-1476.
 23. Kharisov, B.I., *A review for synthesis of nanoflowers*. Recent patents on nanotechnology, 2008. **2**(3): p. 190-200.
 24. Müller, K., et al., *Review on the processing and properties of polymer nanocomposites and nanocoatings and their applications in the packaging, automotive and solar energy fields*. Nanomaterials, 2017. **7**(4): p. 74.
 25. Bugnicourt, E., *Development of sub-micro structured composites based on an epoxy matrix and pyrogenic silica: mechanical behavior related to the interactions and morphology at multi-scale*. 2005, Lyon, INSA.
 26. Niessner, N. and H. Gausepohl, *Polystyrene and styrene copolymers—an overview*. Modern styrenic polymers: poly styrenes and styrenic copolymers. Wiltshire: John Wiley & Sons, 2003: p. 25-42.
 27. Maul, J., et al., *Polystyrene and styrene copolymers*. Ullmann's encyclopedia of industrial chemistry, 2000.
 28. Froese, R., *Insulating properties of styrofoam boxes used for transporting live fish*. Aquaculture, 1998. **159**(3-4): p. 283-292.
 29. Scheirs, J., *Historical overview of styrenic polymers*. Modern styrenic polymers: Polystyrenes and styrenic copolymers, 2003. **6**: p. 1.

30. Scheirs, J. and D. Priddy, *Modern styrenic polymers: polystyrenes and styrenic copolymers*. Vol. 6. 2003: John Wiley & Sons.
31. Ayers, G.W., *Process for removing metal contaminants from petroleum oil*. 1963, Google Patents.
32. Kondoh, G., S. Honda, and Y. Murakami, *Method for removal of oils floating on surface of water*. 1970, Google Patents.
33. Zhu, H., et al., *Evaluation of electrospun polyvinyl chloride/polystyrene fibers as sorbent materials for oil spill cleanup*. *Environmental science & technology*, 2011. **45**(10): p. 4527-4531.
34. Lin, J., et al., *Nanoporous polystyrene fibers for oil spill cleanup*. *Marine pollution bulletin*, 2012. **64**(2): p. 347-352.
35. Wu, J., et al., *CNTs reinforced super-hydrophobic-oleophilic electrospun polystyrene oil sorbent for enhanced sorption capacity and reusability*. *Chemical Engineering Journal*, 2017. **314**: p. 526-536.
36. Alishahi, E., et al., *Effects of carbon nanoreinforcements of different shapes on the mechanical properties of epoxy-based nanocomposites*. *Macromolecular Materials and Engineering*, 2013. **298**(6): p. 670-678.
37. Kayvani Fard, A., et al., *Enhancing oil removal from water using ferric oxide nanoparticles doped carbon nanotubes adsorbents*. *Chemical Engineering Journal*, 2016. **293**: p. 90-101.
38. Ahmadpour, A., N. Eftekhari, and A. Ayati, *Performance of MWCNTs and a low-cost adsorbent for Chromium(VI) ion removal*. *Journal of Nanostructure in Chemistry*, 2014. **4**(4): p. 171-178.
39. Kratochvíla, J., A. Boudenne, and I. Krupa, *Effect of filler size on thermophysical and electrical behavior of nanocomposites based on expanded*

- graphite nanoparticles filled in low-density polyethylene matrix*. Polymer Composites, 2013. **34**(2): p. 149-155.
40. Hadden, C., et al., *Molecular modeling of EPON-862/graphite composites: interfacial characteristics for multiple crosslink densities*. Composites Science and Technology, 2013. **76**: p. 92-99.
 41. Buryachenko, V., et al., *Multi-scale mechanics of nanocomposites including interface: experimental and numerical investigation*. Composites Science and Technology, 2005. **65**(15-16): p. 2435-2465.
 42. Bhuiyan, M.A., et al., *Tensile modulus of carbon nanotube/polypropylene composites—A computational study based on experimental characterization*. Computational Materials Science, 2011. **50**(8): p. 2347-2353.
 43. Xiong, H.-M., et al., *Stable Aqueous ZnO@Polymer Core–Shell Nanoparticles with Tunable Photoluminescence and Their Application in Cell Imaging*. Journal of the American Chemical Society, 2008. **130**(24): p. 7522-7523.
 44. Matei, A., et al., *Synthesis and characterization of ZnO–polymer nanocomposites*. International Journal of Material Forming, 2008. **1**(1): p. 767-770.
 45. Baxter, J.B. and E.S. Aydil, *Metallorganic chemical vapor deposition of ZnO nanowires from zinc acetylacetonate and oxygen*. Journal of the Electrochemical Society, 2009. **156**(1): p. H52-H58.
 46. Vafaei, M. and M.S. Ghamsari, *Preparation and characterization of ZnO nanoparticles by a novel sol–gel route*. Materials Letters, 2007. **61**(14-15): p. 3265-3268.
 47. Wu, J.-J. and S.-C. Liu, *Catalyst-free growth and characterization of ZnO nanorods*. The Journal of Physical Chemistry B, 2002. **106**(37): p. 9546-9551.

48. Vafaei, M. and M.S. Ghamsari, *Preparation and characterization of ZnO nanoparticles by a novel sol-gel route*. Materials Letters, 2007. **61**(14): p. 3265-3268.
49. Park, S.K., K. Do Kim, and H.T. Kim, *Preparation of silica nanoparticles: determination of the optimal synthesis conditions for small and uniform particles*. Colloids and Surfaces A: Physicochemical and Engineering Aspects, 2002. **197**(1-3): p. 7-17.
50. Acierno, D., et al., *Rheological and heat transfer aspects of the melt spinning of monofilament fibers of polyethylene and polystyrene*. Journal of Applied Polymer Science, 1971. **15**(10): p. 2395-2415.
51. Alsalhy, Q.F., *Hollow fiber ultrafiltration membranes prepared from blends of poly (vinyl chloride) and polystyrene*. Desalination, 2012. **294**: p. 44-52.
52. Jarusuwannapoom, T., et al., *Effect of solvents on electro-spinnability of polystyrene solutions and morphological appearance of resulting electrospun polystyrene fibers*. European Polymer Journal, 2005. **41**(3): p. 409-421.
53. Qin, J.-J., J. Gu, and T.-S. Chung, *Effect of wet and dry-jet wet spinning on the shear-induced orientation during the formation of ultrafiltration hollow fiber membranes*. Journal of Membrane Science, 2001. **182**(1-2): p. 57-75.
54. Greiner, A. and J.H. Wendorff, *Electrospinning: a fascinating method for the preparation of ultrathin fibers*. Angewandte Chemie International Edition, 2007. **46**(30): p. 5670-5703.
55. Lee, K.H., et al., *Influence of a mixing solvent with tetrahydrofuran and N, N-dimethylformamide on electrospun poly (vinyl chloride) nonwoven mats*. Journal of polymer science part B: polymer physics, 2002. **40**(19): p. 2259-2268.

56. Lu, X., et al., *Room temperature ionic liquid based polystyrene nanofibers with superhydrophobicity and conductivity produced by electrospinning*. *Chemistry of Materials*, 2008. **20**(10): p. 3420-3424.
57. Gupta, P., et al., *Superparamagnetic flexible substrates based on submicron electrospun Estane® fibers containing MnZnFe□ Ni nanoparticles*. 2006. **100**(6): p. 4935-4942.
58. Ramakrishna, S., et al., *An introduction to nanofibers*. 2005, World Scientific Co., Pte. Ltd., Singapore.
59. Gogotsi, Y., *Nanomaterials handbook*. 2006: CRC press.
60. Asmatulu, R., et al., *Synthesizing magnetic nanocomposite fibers for undergraduate nanotechnology laboratory*. 2010. **38**(3): p. 196-203.
61. Sarkar, K., et al., *Numerical Simulation of Formation and Distortion of Taylor Cones*. 2012. **3**(4): p. 041001.
62. Reneker, D.H., et al., *Bending instability of electrically charged liquid jets of polymer solutions in electrospinning*. 2000. **87**(9): p. 4531-4547.
63. Burger, C., B.S. Hsiao, and B.J.A.R.M.R. Chu, *Nanofibrous materials and their applications*. 2006. **36**: p. 333-368.
64. Teo, W.E. and S.J.N. Ramakrishna, *A review on electrospinning design and nanofibre assemblies*. 2006. **17**(14): p. R89.
65. Li, D. and Y.J.A.m. Xia, *Electrospinning of nanofibers: reinventing the wheel?* 2004. **16**(14): p. 1151-1170.
66. Koombhongse, S., W. Liu, and D.H.J.J.o.P.S.P.B.P.P. Reneker, *Flat polymer ribbons and other shapes by electrospinning*. 2001. **39**(21): p. 2598-2606.
67. Mo, X., et al., *Electrospun P (LLA-CL) nanofiber: a biomimetic extracellular matrix for smooth muscle cell and endothelial cell proliferation*. 2004. **25**(10):

- p. 1883-1890.
68. El-Samak, A.A., et al., *Designing Flexible and Porous Fibrous Membranes for Oil Water Separation—A Review of Recent Developments*. *Polymer Reviews*, 2020: p. 1-46.
 69. Ma, M. and R.M. Hill, *Superhydrophobic surfaces*. *Current opinion in colloid & interface science*, 2006. **11**(4): p. 193-202.
 70. Kota, A.K., J.M. Mabry, and A. Tuteja, *Superoleophobic surfaces: design criteria and recent studies*. *Surface Innovations*, 2013. **1**(2): p. 71-83.
 71. Wang, Z., M. Elimelech, and S. Lin, *Environmental applications of interfacial materials with special wettability*. *Environmental science & technology*, 2016. **50**(5): p. 2132-2150.
 72. Adebajo, M.O., et al., *Porous Materials for Oil Spill Cleanup: A Review of Synthesis and Absorbing Properties*. *Journal of Porous Materials*, 2003. **10**(3): p. 159-170.
 73. Pintor, A.M., et al., *Oil and grease removal from wastewaters: sorption treatment as an alternative to state-of-the-art technologies. A critical review*. 2016. **297**: p. 229-255.
 74. Sokker, H.H., et al., *Adsorption of crude oil from aqueous solution by hydrogel of chitosan based polyacrylamide prepared by radiation induced graft polymerization*. *Journal of Hazardous Materials*, 2011. **190**(1): p. 359-365.
 75. Carmody, O., et al., *Adsorption of hydrocarbons on organo-clays—Implications for oil spill remediation*. *Journal of Colloid and Interface Science*, 2007. **305**(1): p. 17-24.
 76. Ceylan, D., et al., *Evaluation of butyl rubber as sorbent material for the removal of oil and polycyclic aromatic hydrocarbons from seawater*. *Environmental*

- science & technology, 2009. **43**(10): p. 3846-3852.
77. Karakutuk, I. and O. Okay, *Macroporous rubber gels as reusable sorbents for the removal of oil from surface waters*. Reactive and Functional Polymers, 2010. **70**(9): p. 585-595.
 78. Srinivasan, A. and T. Viraraghavan, *Removal of oil by walnut shell media*. Bioresource technology, 2008. **99**(17): p. 8217-8220.
 79. Al-Majed, A.A., A.R. Adebayo, and M.E. Hossain, *A sustainable approach to controlling oil spills*. Journal of Environmental Management, 2012. **113**: p. 213-227.
 80. Li, A., et al., *Superhydrophobic conjugated microporous polymers for separation and adsorption*. Energy & Environmental Science, 2011. **4**(6): p. 2062-2065.
 81. Annunciado, T., T. Sydenstricker, and S. Amico, *Experimental investigation of various vegetable fibers as sorbent materials for oil spills*. Marine pollution bulletin, 2005. **50**(11): p. 1340-1346.
 82. Wahi, R., et al., *Oil removal from aqueous state by natural fibrous sorbent: an overview*. Separation and Purification Technology, 2013. **113**: p. 51-63.
 83. Ribeiro, T.H., J. Rubio, and R.W. Smith, *A dried hydrophobic aquaphyte as an oil filter for oil/water emulsions*. Spill science & technology bulletin, 2003. **8**(5-6): p. 483-489.
 84. Niederberger, M., *Nonaqueous Sol–Gel Routes to Metal Oxide Nanoparticles*. Accounts of Chemical Research, 2007. **40**(9): p. 793-800.
 85. Katsogiannis, K.A.G., G.T. Vladislavljević, and S.J.E.P.J. Georgiadou, *Porous electrospun polycaprolactone (PCL) fibres by phase separation*. 2015. **69**: p. 284-295.

86. Wei, Z., et al., *Porous electrospun ultrafine fibers via a liquid–liquid phase separation method*. 2013. **291**(5): p. 1293-1296.
87. Garg, K. and G.L.J.B. Bowlin, *Electrospinning jets and nanofibrous structures*. 2011. **5**(1): p. 013403.
88. Bartels, W.J., *Characterization of thin layers on perfect crystals with a multipurpose high resolution x-ray diffractometer*. 1983. **1**(2): p. 338-345.
89. Stanjek, H. and W.J.H.I. Häusler, *Basics of X-ray Diffraction*. 2004. **154**(1): p. 107-119.
90. Polini, A. and F. Yang, *Physicochemical characterization of nanofiber composites*, in *Nanofiber Composites for Biomedical Applications*. 2017, Elsevier. p. 97-115.
91. ROSENBERG, M., I.J. KOPELMAN, and Y. TALMON, *A Scanning Electron Microscopy Study of Microencapsulation*. 1985. **50**(1): p. 139-144.
92. Duan, Y.-y., et al., *Preparation of antimicrobial poly(ϵ -caprolactone) electrospun nanofibers containing silver-loaded zirconium phosphate nanoparticles*. 2007. **106**(2): p. 1208-1214.
93. Reimer, L., *Transmission electron microscopy: physics of image formation and microanalysis*. Vol. 36. 2013: Springer.
94. Tjong, S.C., *Structural and mechanical properties of polymer nanocomposites*. Materials Science and Engineering: R: Reports, 2006. **53**(3-4): p. 73-197.
95. Wunderlich, B., *Thermal analysis of polymeric materials*. 2005: Springer Science & Business Media.
96. Wenzel, R.N., *Surface roughness and contact angle*. The Journal of Physical Chemistry, 1949. **53**(9): p. 1466-1467.
97. Cho, E.-C., et al., *Robust multifunctional superhydrophobic coatings with*

- enhanced water/oil separation, self-cleaning, anti-corrosion, and anti-biological adhesion.* Chemical Engineering Journal, 2017. **314**: p. 347-357.
98. Sabri, S., et al., *Antibacterial Properties of Polysulfone Membranes Blended with Arabic Gum.* 2019. **9**(2): p. 29.
 99. Becheri, A., et al., *Synthesis and characterization of zinc oxide nanoparticles: application to textiles as UV-absorbers.* 2008. **10**(4): p. 679-689.
 100. Ibrahim, A.A., et al., *Growth and properties of Ag-doped ZnO nanoflowers for highly sensitive phenyl hydrazine chemical sensor application.* Talanta, 2012. **93**: p. 257-263.
 101. Karunakaran, C., V. Rajeswari, and P. Gomathisankar, *Antibacterial and photocatalytic activities of sonochemically prepared ZnO and Ag-ZnO.* Journal of Alloys and Compounds, 2010. **508**(2): p. 587-591.
 102. Khosravi-Gandomani, S., et al., *Optical and electrical properties of p-type Ag-doped ZnO nanostructures.* Ceramics international, 2014. **40**(6): p. 7957-7963.
 103. Parangusan, H., D. Ponnamma, and M.A.A. Al-Maadeed, *Effect of cerium doping on the optical and photocatalytic properties of ZnO nanoflowers.* Bulletin of Materials Science, 2019. **42**(4): p. 179.
 104. Hosseini, S., et al., *Effect of Ag doping on structural, optical, and photocatalytic properties of ZnO nanoparticles.* Journal of Alloys and Compounds, 2015. **640**: p. 408-415.
 105. Murtaza, G., et al., *Structural and magnetic studies on Zr doped ZnO diluted magnetic semiconductor.* Current Applied Physics, 2014. **14**(2): p. 176-181.
 106. Zang, Z., et al., *Strong yellow emission of ZnO hollow nanospheres fabricated using polystyrene spheres as templates.* Materials & Design, 2015. **84**: p. 418-421.

107. Jeeju, P. and S. Jayalekshmi, *On the interesting optical properties of highly transparent, thermally stable, spin-coated polystyrene/zinc oxide nanocomposite films*. Journal of applied polymer science, 2011. **120**(3): p. 1361-1366.
108. Chae, D.W. and B.C. Kim, *Characterization on polystyrene/zinc oxide nanocomposites prepared from solution mixing*. Polymers for advanced technologies, 2005. **16**(11-12): p. 846-850.
109. Ma, C.C.M., Y.J. Chen, and H.C. Kuan, *Polystyrene nanocomposite materials—preparation, mechanical, electrical and thermal properties, and morphology*. Journal of applied polymer science, 2006. **100**(1): p. 508-515.
110. Yıldırım, Ö.A., H.E. Unalan, and C. Durucan, *Highly efficient room temperature synthesis of silver-doped zinc oxide (ZnO: Ag) nanoparticles: structural, optical, and photocatalytic properties*. Journal of the American Ceramic Society, 2013. **96**(3): p. 766-773.
111. Wu, J., et al., *Electrospun porous structure fibrous film with high oil adsorption capacity*. ACS applied materials & interfaces, 2012. **4**(6): p. 3207-3212.
112. Ponnamma, D., et al., *Smart and robust electrospun fabrics of piezoelectric polymer nanocomposite for self-powering electronic textiles*. Materials & Design, 2019. **184**: p. 108176.
113. Augustine, R., et al., *Electrospun polycaprolactone/ZnO nanocomposite membranes as biomaterials with antibacterial and cell adhesion properties*. Journal of Polymer Research, 2014. **21**(3): p. 347.
114. Ma, G., D. Yang, and J. Nie, *Preparation of porous ultrafine polyacrylonitrile (PAN) fibers by electrospinning*. Polymers for Advanced Technologies, 2009. **20**(2): p. 147-150.

115. Zong, X., et al., *Structure and process relationship of electrospun bioabsorbable nanofiber membranes*. Polymer, 2002. **43**(16): p. 4403-4412.
116. Wang, Z., et al., *Ag-nanoparticle-decorated porous ZnO-nanosheets grafted on a carbon fiber cloth as effective SERS substrates*. Nanoscale, 2014. **6**(24): p. 15280-15285.
117. Wei, W., et al., *Improving the Damping Properties of Nanocomposites by Monodispersed Hybrid POSS Nanoparticles: Preparation and Mechanisms*. Polymers, 2019. **11**(4): p. 647.
118. Mansour, S.A., *Study of thermal stabilization for polystyrene/carbon nanocomposites via TG/DSC techniques*. Journal of thermal analysis and calorimetry, 2013. **112**(2): p. 579-583.
119. Ponnamma, D., et al., *Free-volume correlation with mechanical and dielectric properties of natural rubber/multi walled carbon nanotubes composites*. Composites Part A: Applied Science and Manufacturing, 2015. **77**: p. 164-171.
120. Devi, K.U., et al., *Enhanced morphology and mechanical characteristics of clay/styrene butadiene rubber nanocomposites*. Applied clay science, 2015. **114**: p. 568-576.
121. Abdelrazeq, H., et al., *Recycled Polyethylene/Paraffin Wax/Expanded Graphite Based Heat Absorbers for Thermal Energy Storage: An Artificial Aging Study*. Molecules, 2019. **24**.
122. Ponnamma, D., et al., *Developing Polyaniline Filled Isoprene Composite Fibers by Electrospinning: Effect of Filler Concentration on the Morphology and Glass Transition*. Polymer Science, Series A, 2019. **61**: p. 194-202.
123. Lee, I., et al., *Interfacial toughening of solution processed Ag nanoparticle thin films by organic residuals*. Nanotechnology, 2012. **23**(48): p. 485704.

124. Tang, E. and S. Dong, *Preparation of styrene polymer/ZnO nanocomposite latex via miniemulsion polymerization and its antibacterial property*. Colloid and Polymer Science, 2009. **287**(9): p. 1025-1032.
125. Montazer, M. and T. Harifi, *9 - Nanofinishes for self-cleaning textiles*, in *Nanofinishing of Textile Materials*, M. Montazer and T. Harifi, Editors. 2018, Woodhead Publishing. p. 127-143.
126. Wang, X., et al., *Engineering biomimetic superhydrophobic surfaces of electrospun nanomaterials*. Nano today, 2011. **6**(5): p. 510-530.
127. Bahgat, A., et al., *Corrosion Protection of Electrospun PVDF-ZnO Superhydrophobic Coating*. Surface and Coatings Technology, 2015. **289**.
128. Duong, H.T. and R.P. Burford, *Effect of foam density, oil viscosity, and temperature on oil sorption behavior of polyurethane*. Journal of applied polymer science, 2006. **99**(1): p. 360-367.
129. Lin, J., et al., *Co-axial electrospun polystyrene/polyurethane fibres for oil collection from water surface*. Nanoscale, 2013. **5**(7): p. 2745-2755.
130. Youssef, A.M., S. Kamel, and M. El-Samahy, *Morphological and antibacterial properties of modified paper by PS nanocomposites for packaging applications*. Carbohydrate polymers, 2013. **98**(1): p. 1166-1172.
131. ALzubaidy, Z.M., N.M. Amin, and M. Sabah, *The Antibacterial Effect of Silver and Zinc Oxide Nanoparticles against Intracellular Brucella melitensis*. International Journal of Medical Sciences, 2019. **2**(1): p. 29-42.
132. Rastogi, S.K., et al., *Ag colloids and Ag clusters over EDAPTMS-coated silica nanoparticles: synthesis, characterization, and antibacterial activity against Escherichia coli*. Nanomedicine: Nanotechnology, Biology and Medicine, 2011. **7**(3): p. 305-314.

133. Salomoni, R., et al., *Antibacterial effect of silver nanoparticles in Pseudomonas aeruginosa*. Nanotechnology, science and applications, 2017. **10**: p. 115.
134. Ong, C.B., L.Y. Ng, and A.W. Mohammad, *A review of ZnO nanoparticles as solar photocatalysts: Synthesis, mechanisms and applications*. Renewable and Sustainable Energy Reviews, 2018. **81**: p. 536-551.
135. Sirbu, D., et al., *Rosindone revisited: a computational and photophysical study of 7-phenylbenzo[a]phenazine-5(7H)-one (PBP)*. Photochemical & Photobiological Sciences, 2019. **18**(1): p. 140-147.
136. Divband, B., et al., *Synthesis of Ag/ZnO nanostructures by different methods and investigation of their photocatalytic efficiency for 4-nitrophenol degradation*. Applied Surface Science, 2013. **284**: p. 80-86.